

1     **The role of anthropogenic aerosols in the anomalous cooling**  
2             **from 1960 to 1990 in the CMIP6 Earth System Models**

3     Jie Zhang<sup>1</sup>, Kalli Furtado<sup>2\*</sup>, Steven T. Turnock<sup>2</sup>, Jane P. Mulcahy<sup>2</sup>, Laura J. Wilcox<sup>3</sup>,  
4             Ben B. Booth<sup>2</sup>, David Sexton<sup>2</sup>, Tongwen Wu<sup>1</sup>, Fang Zhang<sup>1</sup>, Qianxia Liu<sup>1</sup>

5     <sup>1</sup>Beijing Climate Center, China Meteorological Administration, Beijing, China, 100081

6     <sup>2</sup>Met Office Hadley Centre, Exeter, UK, EX1 3PB

7     <sup>3</sup>National Centre for Atmospheric Science, Department of Meteorology, University of Reading, Reading,  
8     UK

9     *Corresponding to:* Kalli Furtado (kalli.furtado@metoffice.gov.uk)

10

11     **Abstract** The Earth System Models (ESMs) that participated in the 6<sup>th</sup> Coupled Model  
12     Intercomparison Project (CMIP6) tend to simulate excessive cooling in surface air  
13     temperature (TAS) between 1960 and 1990. The anomalous cooling is pronounced over  
14     the Northern Hemisphere (NH) midlatitudes, coinciding with the rapid growth of  
15     anthropogenic sulfur dioxide (SO<sub>2</sub>) emissions, the primary precursor of atmospheric  
16     sulphate aerosols. Structural uncertainties between ESMs have a larger impact on the  
17     anomalous cooling than internal variability. Historical simulations with and without  
18     anthropogenic aerosol emissions indicate that the anomalous cooling in the ESMs is  
19     attributed to the higher aerosol burden in these models. The aerosol-forcing sensitivity,  
20     estimated as the outgoing shortwave radiation (OSR) response to aerosol concentration  
21     changes, cannot well explain the diversity of PHC biases in the ESMs. The relative  
22     contributions to aerosol-forcing-sensitivity from aerosol-radiation interactions (ARI)  
23     and aerosol-cloud interactions (ACI) can be estimated from CMIP6 simulations. We  
24     show that even when the aerosol-forcing-sensitivity is similar between ESMs, the  
25     relative contributions of ARI and ACI may be substantially different. The ACI accounts  
26     for between 64 to 87% of the aerosol-forcing-sensitivity in the models, and is the main  
27     source of the aerosol-forcing sensitivity differences between the ESMs. The ACI can  
28     be further decomposed into a cloud-amount term (which depends linearly on cloud  
29     fraction) and a cloud-albedo term (which is independent of cloud fraction, to the first  
30     order) with the cloud-amount term accounting for most of the inter-model differences.

## 31 **1. Introduction**

32 Surface air temperature (TAS) variation is an essential indicator of climate change,  
33 and reproducing the evolution of historical TAS is a crucial criterion for model  
34 evaluation. However, the historical TAS anomaly simulated by the models in the 6<sup>th</sup>  
35 Coupled Model Intercomparison Project (CMIP6) is on average colder than that  
36 observed in the mid-twentieth century, whereas the CMIP5 models tracked the  
37 instrumental TAS variation quite well (Flynn and Mauritsen, 2020). This is surprising  
38 because the transient climate response in CMIP6 models is generally higher than in  
39 CMIP5 models (e.g., Flynn and Mauritsen, 2020; Meehl et al., 2020).

40 As a result of anthropogenic emissions, atmospheric aerosol concentrations  
41 increased along with rising greenhouse gases, but with greater decadal variability.  
42 Aerosols are generally not evenly distributed around the planet as greenhouse gases,  
43 and they have relatively short lifetimes of the order of a week. Aerosols increased  
44 rapidly in the mid-twentieth century, predominantly due to US and European emissions.  
45 The rate of change of global aerosol emissions slowed down in the late 20<sup>th</sup> century  
46 (Hoesly et al., 2018), and the trend of global emission has been negative since the mid-  
47 2000s (Klimont et al., 2013). There has also been a shift in emission source regions.  
48 European and US emissions have declined following the introduction of clean air  
49 legislation since the 1980s, while Asian emissions have risen due to economic  
50 development. East Asian emissions clearly increased from 2000 to 2005, followed by  
51 a decrease with large uncertainties (Aas et al., 2020). The decade long emission  
52 reduction since 2006 over East China is not well represented by the CMIP6 emission  
53 (Wang et al., 2021).

54 Although greenhouse warming was concluded to be the dominant forcing for long-  
55 term changes (e.g., Weart, 2008; Bindoff et al., 2013), multidecadal variability in TAS  
56 and the reduced rate of warming in the mid-twentieth century in particular, has been  
57 attributed to aerosol forcing (e.g., Wilcox et al., 2013). Ramanathan and Feng (2009)  
58 noted that the aerosol cooling effect might have masked as much as 47% of the global  
59 warming by greenhouse gases in the year 2005, with an uncertainty range of 20~80%.

60 The aerosol cooling effect is mainly attributed to the ability of sulphate particles to  
61 reflect incoming solar radiation and modify the microphysical properties of clouds (e.g.,  
62 Charlson et al., 1990; Mitchell et al., 1995; Lohmann and Feichter, 2005). The increase  
63 in anthropogenic aerosols was also responsible for weakening the hydrological cycle  
64 between the 1950s and the 1980s (Wu et al., 2013).

65 Previous work has suggested that the anomalous mid-twentieth century cooling in  
66 the CMIP6 models is the result of excessive aerosol forcing. Flynn and Mauritsen  
67 (2020) suggested that aerosol cooling is too strong in many CMIP6 models because  
68 there is no apparent relationship between the warming trends simulated by models and  
69 their transient climate responses (TCRs) before the 1970s. Dittus et al. (2020) found  
70 that historical simulations can better capture the observed historical record by reducing  
71 the aerosol emissions in HadGEM3-GC3.1, demonstrating an overly strong aerosol  
72 cooling effect. In this study we characterize the mid-twentieth century excessive  
73 cooling in CMIP6 ESMs. In order to quantify the role of aerosol processes in this  
74 anomalous cooling, historical experiments with and without anthropogenic aerosol  
75 emissions are employed. The remainder of the paper is organized as follows. Section 2  
76 introduces the models, data, and a quantitative method to separate the aerosol forcing  
77 components. The major features of anomalous cooling in CMIP6 ESMs are examined  
78 in section 3. Section 4 investigates the possible reasons for the anomalous cooling. The  
79 relative importance of aerosol-radiation interactions and aerosol-cloud interactions in  
80 each ESM is quantified and discussed in section 5. Conclusion is given in Section 6.

81

## 82 **2. Model, data, and method**

### 83 **2.1 CMIP6 ESMs**

84 CMIP6 includes an unprecedented number of models with representations of  
85 aerosol-cloud interactions. Many also have interactive tropospheric chemistry and  
86 aerosol schemes. Six such ESMs are employed in this study: BCC-ESM1 (Wu et al.,  
87 2020; Zhang et al., 2021), EC-Earth-AerChem (van Noije et al., 2020), GFDL-ESM4  
88 (Dunne et al., 2020), MPI-ESM-1-2-HAM (Neubauer et al., 2019), NorESM2-LM

89 (Seland et al., 2020), and UKESM1-0-LL (Sellar et al., 2019). The surface air  
90 temperature simulated in corresponding models with lower-complexity are also  
91 examined: BCC-CSM2-MR (Wu et al., 2019b), EC-Earth3 (Döscher et al., 2021), and  
92 MPI-ESM1-2-LR (Mauritsen et al., 2019) with prescribed tropospheric chemistry and  
93 aerosol; GFDL-CM4 (Held et al., 2019), NorCPM1 (Bethke et al., 2019), and  
94 HadGEM3-GC31-LL (Williams et al., 2017) with prescribed tropospheric chemistry  
95 and interactive aerosol scheme. BCC-CSM2-MR, EC-Earth3, and MPI-ESM1-2-LR  
96 prescribe the anthropogenic aerosol forcings using the MACv2-SP parameterization  
97 (Stevens et al., 2017). MACv2-SP approximates the observationally constrained spatial  
98 distributions of the monthly mean anthropogenic aerosol optical properties and an  
99 associated Twomey effect. A brief summary of the ESMs and the lower-complexity  
100 models is introduced in Table 1.

101 **Table 1.** Information of the ESMs with interactive chemistry and aerosol scheme, as  
 102 well as the corresponding lower-complexity models.

| Modeling group  | ESM<br>(Atmospheric<br>Resolution)  | Lower-complexity<br>models<br>(Atmospheric<br>Resolution)   | Prescribed<br>tropospheric<br>chemistry | Prescribed<br>aerosol | Number<br>of<br>members | References                                      |
|---|---|---|---|-----------------------|-------------------------|---|
| Beijing Climate Center (BCC)  | <b>BCC-ESM1:</b> the BCC Earth System Model version 1 (T42, 26 layers to 2.914 hPa)   | <b>BCC-CSM2-MR:</b> the median resolution BCC Climate System Model version 2 (T106, 46 layers to 1.459 hPa)                         | Y                                       | Y                     | 3                       | Wu et al.(2019b, 2020); Zhang et al. (2021)     |
| European consortium of meteorological services, research institutes, and high-performance computing centres | <b>EC-Earth-AerChem:</b> the EC-Earth configuration with interactive aerosols and atmospheric chemistry (T255, 91 layers to 0.01 hPa) | <b>EC-Earth3:</b> the EC-Earth version 3 (T255, 91 layers to 0.01 hPa)  | Y                                       | Y                     | 1                       | von Noije et al. (2020); Döscher et al. (2021)  |
| US Department of Commerce/NOAA / Geophysical Fluid Dynamics Laboratory (GFDL)                               | <b>GFDL-ESM4:</b> the GFDL Earth System Model version 4 (C96, 49 layers to 1 hPa)   | <b>GFDL-CM4:</b> the GFDL Climate Model version 4 (C96, 33 layers to 1 hPa)   | Y                                       | N                     | 1                       | Dunne et al. (2020); Held et al. (2019)         |
| Max Planck Institute for Meteorology (MPI)  | <b>MPI-ESM-1-2-HAM:</b> the HAMMOZ-Consortium of MPI Earth System Model (T63, 47 layers to 0.01 hPa)                                  | <b>MPI-ESM1-2-LR:</b> the lower-resolution version of MPI Earth System Model (T63, 47 layers to 0.01 hPa)                           | Y                                       | Y                     | 3                       | Neubauer et al.(2019); Mauritsen et al. (2019); |
| Norwegian Climate Center (NCC)  | <b>NorESM2-LM:</b> the lower-resolution of Norwegian ESM version 2 (About 2°, 32 layers to 2 hPa)                                     | <b>NorCPM1:</b> the Norwegian Climate Prediction Model version 1 (About 2°, 26 layers to 3 hPa)                                     | Y                                       | N                     | 3                       | Seland et al. (2020); Bethke et al. (2019)      |
| Met Office’s Hadley Centre for Climate Prediction and Research (MOHC)                                       | <b>UKESM1-0-LL:</b> U.K. Earth System Model version 1 (N96, 85 layers to 85 km)   | <b>HadGEM3-GC31-LL:</b> the Hadley Centre Global Environment Model in the Global Coupled configuration 3.1 (N96, 85 layers to 85km) | Y                                       | N                     | 3                       | Sellar et al. (2019); Williams et al. (2017)    |

104 **2.2 Data**

105

106

**Table 2** Variables used in this study.

| <b>Variable name</b> | <b>CMIP6 diagnostic label</b> | <b>Description</b>  | <b>Units</b>        |
|----------------------|-------------------------------|---|---------------------|
| TAS                  | tas                           | Surface air temperature   | °C                  |
| OSR                  | rsut                          | All-sky outgoing shortwave radiation at the top of atmosphere (TOA) | W m <sup>-2</sup>   |
| OSRclr               | rsutcs                        | OSR assuming clear sky  | W m <sup>-2</sup>   |
| mmrso4               | mmrso4                        | Mass mixing ratio of sulphate aerosol in the atmosphere             | kg kg <sup>-1</sup> |
| CLT                  | clt                           | Total cloud amount  | %                   |
| r <sub>eff</sub>     | reffcldwtop                   | cloud-top effective droplet radius                                  | µm                  |
| loadSO4              |                               | Sulphate loading in the atmosphere, calculated from mmrso4          | mg m <sup>-2</sup>  |
| OSRclr_hist          |                               | Mean OSRclr in the historical simulation from 1850 to 1990          | W m <sup>-2</sup>   |
| CLT_hist             |                               | Mean CLT in the historical simulation from 1850 to 1990             | %                   |

107

108 The CMIP6 historical experiment and hist-piAer experiment are employed. The  
 109 historical experiment is forced by time-evolving, externally imposed natural and  
 110 anthropogenic forcings, such as solar variability, volcanic aerosols, greenhouse gases,  
 111 and aerosol emissions (Eyring et al., 2016). The hist-piAer experiment is designed by  
 112 the CMIP6-endorsed Aerosol Chemistry Model Intercomparison Project  
 113 (AerChemMIP; Collins et al., 2017). It is run in parallel with the historical experiment  
 114 but fixes aerosol and aerosol precursor emissions to pre-industrial conditions.  
 115 Therefore, the differences between these two experiments are attributable to  
 116 anthropogenic aerosol emissions. The design of the hist-piAer simulation means that it

117 can also capture any nonlinearities resulting from GHG-driven changes in clouds. This  
118 is in contrast to the hist-aer simulations available from the Detection and Attribution  
119 Model Intercomparison Project (DAMIP; Gillett et al., 2016), which resembles the  
120 historical simulations but are only forced by transient changes in aerosol.

121 The monthly outputs from historical and hist-piAer simulations for ESMs are used,  
122 including TAS, all-sky outgoing shortwave radiation at the top-of-atmosphere (OSR),  
123 OSR assuming clear sky (OSRclr), mass mixing ratio of sulphate aerosol in the  
124 atmosphere (mmrso4), total cloud amount (CLT), and cloud-top effective droplet radius  
125 ( $r_{\text{eff}}$ ). These variables are summarized in Table 2. The corresponding lower-complexity  
126 models have conducted the historical but not the hist-piAer simulations, and only the  
127 monthly TAS output from the historical simulations are used. Therefore, we focus on  
128 the ESMs when identifying the main aerosol processes contributing to the anomalous  
129 cooling.

130 The verification data used in this study is HadCRUT5, the monthly 5°lat by 5°lon  
131 gridded surface temperature (Morice et al., 2021), a blend of the Met Office Hadley  
132 Centre SST data set HadSST4 (Kennedy et al., 2019) and the land surface air  
133 temperature CRUTEM5 (Osborn et al., 2021).

134

### 135 **2.3 Method**

136 By comparing the TAS anomalies in ESMs and the lower-complexity models with  
137 HadCRUT5, our study found that TAS anomalies from 1960 to 1990 relative to 1850-  
138 1900 in ESMs and most of the lower-complexity models are on average much lower  
139 than observed, resembling a "pot-hole" shape. The magnitude of this anomalous  
140 cooling, i.e., the "pot-hole" cooling (PHC), is quantified as the near-global mean (60°S  
141 to 65°N) difference in the TAS anomaly between models and HadCRUT5 from 1960  
142 to 1990. The variations over the polar regions (north of 65°N and south of 60°S) are not  
143 considered due to the lack of long-term reliable observations (Wu et al., 2019a).

144 The aerosol cooling is dominated by the contribution of sulphate aerosol as

145 estimated by models and observations (Myhre et al., 2013; Smith et al., 2020). We use  
146 the evolution of sulphate loading ( $loadSO_4$ ) through the historic simulation as a proxy  
147 for total aerosol concentration changes to link estimates of the impact of aerosol  
148 forcing. Whilst the overall impact of aerosol forcing will also depend on other aerosol  
149 species, we adopt this approach because the sulphates dominate estimates of aerosol  
150 forcing during this period and other aerosols species can be assumed (as a 1<sup>st</sup> order  
151 approximation) to have covaried with the  $SO_2$  emissions during this period as presented  
152 by the Community Emissions Data System (CEDS) inventory adopted by CMIP6  
153 models (Hoesly et al, 2018). As such when we present estimates of the aerosol  
154 impact/ $loadSO_4$  we are presenting the impact of all aerosol species (including  
155 absorbing aerosols such as black carbon) as they covary with the sulphate  
156 concentrations during the historic period. The motivation for presenting it in this way,  
157 is we can separate differences in ESM responses to changes in aerosol amount from the  
158 differences in aerosol amount (represented by  $loadSO_4$ ) simulated by the ESMs.

159 We can estimate the impact of anthropogenic aerosol by using the difference in  
160 OSR between the historical and hist-piAer simulations,  $\Delta OSR$ .  $\Delta OSR$  of course involves  
161 any differences in natural variability and planetary albedo between the two simulations,  
162 including clear-sky albedo changes and any adjustments in the microphysical or  
163 macroscopic properties of clouds. The sensitivity of the OSR-response to aerosol  
164 changes, i.e., the aerosol-forcing-sensitivity, can be measured by the linear fit slope  
165 between the annual mean globally averaged OSR differences and  $loadSO_4$  differences  
166 between the historical and hist-piAer simulations:

$$167 \quad \text{Aerosol-forcing-sensitivity} = \Delta OSR / \Delta loadSO_4. \quad (1)$$

168

169 In this study, we diagnose the OSR differences from historical simulations that  
170 also capture the temperature response. As such the OSR differences do not represent a  
171 measure of only the aerosol forcing impact but combine OSR differences arising from  
172 both the aerosol forcing and the temperature response to this forcing, which we refer to  
173 in this manuscript as the aerosol-forcing-sensitivity. It presents a measure of the



174 importance of aerosol changes in simulated temperature changes that can be easily  
 175 calculated for existing transient simulations. The aerosol-forcing-sensitivity is different  
 176 from the commonly used aerosol effective radiative forcing (ERFaer), which is the  
 177 change in net TOA downward radiative flux after allowing adjustments in the  
 178 atmosphere, but with sea surface temperatures and sea ice cover are fixed at  
 179 climatological values. The ERFaer for each ESM except MPI-ESM-1-2-HAM is listed  
 180 in Table 3 and compared with the aerosol-forcing-sensitivity in section 4.

181 The aerosol-forcing-sensitivity can be further partitioned into a contribution from  
 182 aerosol-radiation interactions (ARI), and aerosol-cloud interactions (ACI). ARI and  
 183 ACI can be readily estimated from the CMIP6 output because annual mean cloud  
 184 amount (CLT), OSR, and the OSR *assuming only clear-sky* (OSRclr), are available for  
 185 all the CMIP6 ESMs. For each model, the clear-sky part OSR, OSRclr\_p, can be  
 186 estimated as  $(1-CLT/100.) * OSRclr$ . The aerosol-forcing-sensitivity in clear-sky part  
 187 can therefore be estimated as:

$$188 \quad \Delta OSRclr\_p / \Delta loadSO4 = (1-CLT\_hist/100.) * \Delta OSRclr / \Delta loadSO4$$

$$189 \quad - OSRclr\_hist/100 * \Delta CLT / \Delta loadSO4 + residual\_clr, \quad (2)$$

190 where CLT\_hist and OSRclr\_hist are the mean CLT and OSRclr in the historical  
 191 experiment. The aerosol-forcing-sensitivity in cloudy part are relative to cloud amount  
 192 response to aerosol loading and cloud radiative effect changes and can be estimated as:

$$193 \quad \Delta OSRcld\_p / \Delta loadSO4 = A * \Delta CLT / \Delta loadSO4 + cloud-albedo term$$

$$194 \quad + residual\_cld. \quad (3)$$

195 Therefore, the aerosol-forcing-sensitivity can be decomposed as:

$$196 \quad \underbrace{\Delta OSR / \Delta loadSO4}_{Aerosol-forcing-sensitivity} = (1-CLT\_hist/100) * \Delta OSRclr / \Delta loadSO4$$

$$197 \quad + (A-OSRclr\_hist/100.) * \Delta CLT / \Delta loadSO4$$

$$198 \quad + cloud-albedo term + residual$$

$$199 \quad = \underbrace{(1-CLT\_hist/100) * M}_{Aerosol-rad. Interactions (ARI)} + \underbrace{(A-OSRclr\_hist/100.) * N}_{cloud-amount term}$$

$$200$$

201 
$$+ \text{cloud-albedo term} + \text{residual}, \quad (4)$$

202 where M, N and A are empirically determined parameters. The parameter M is the  
 203 slope of a linear fit of  $\Delta\text{OSRclr}$  to  $\Delta\text{loadSO}_4$ , and therefore measures the strength of  
 204 the aerosol-radiation interactions in each model. The first term on the right-hand side  
 205 of Eq. (4),  $(1-\text{CLT}_{\text{hist}}/100.) * M$ , can therefore be identified with ARI. The parameter  
 206 A is the slope of a linear fit of  $\Delta\text{OSRcld}$  to  $\Delta\text{CLT}$ , and therefore measures the  
 207 correlation of the shortwave radiation reflected by clouds with changes in cloud  
 208 amount. That is, the parameter A represents the baseline cloud albedo which is sensitive  
 209 to the cloud parameterizations via Cloud Droplet Number Concentration (CDNC),  
 210 cloud-droplet effective radius, and other factors. The parameter N is the slope of a linear  
 211 fit of  $\Delta\text{CLT}$  to  $\Delta\text{loadSO}_4$ , and therefore measures the sensitivity of cloud amount to  
 212 aerosols. Note that changes in cloud amount by definition also affect the fraction of  
 213 clear-sky, hence increases in OSRcld due to increases in CLT (i.e.,  $A * N$ ) can be partly  
 214 offset by changes in area of clear-sky containing aerosols ( $\text{OSRclr}_{\text{hist}}/100. * N$ ). The  
 215 second term on the right-hand side of Eq. (4),  $(A-\text{OSRclr}_{\text{hist}}/100.) * N$ , can therefore  
 216 contribute to the ACI. Specifically, it is the part of ACI that is linearly proportional to  
 217 changes to cloud fraction, which we will refer to in this manuscript as the cloud-amount  
 218 term. It is therefore sensitive to *any* aerosol-induced cloud fraction changes (Lohmann  
 219 and Feichter, 2005), including any slow adjustments in clouds due to feedbacks within  
 220 the Earth System.

221 In addition to depending on  $\Delta\text{CLT}$ , ACI is also influenced by any changes in  
 222 cloud-albedo that might occur independently of cloud-amount changes. Such  
 223 adjustments would include increases in cloud droplet number concentration and  
 224 increases in simulated cloud-droplet effective radius without accompanying changes in  
 225 cloud cover. Changes purely in the brightness of clouds, without changes in  
 226 macroscopic properties of clouds, are difficult to identify from the CMIP6 output  
 227 because all the bulk-properties of clouds co-vary over the course of the projections.  
 228 However, subtracting ARI and the cloud-amount term from the aerosol-forcing-  
 229 sensitivity gives a residual that is, by definition, linearly independent of cloud fraction

230 differences (since by construction these have been regressed out). This residual can then  
231 be interpreted as due to differences in the albedo of clouds between the historical and  
232 hist-piAer, and will be called the "cloud-albedo term". Note that this method of  
233 calculation implies that purely albedo effects cannot be distinguished from general  
234 residual terms that result from the linear approximation made.

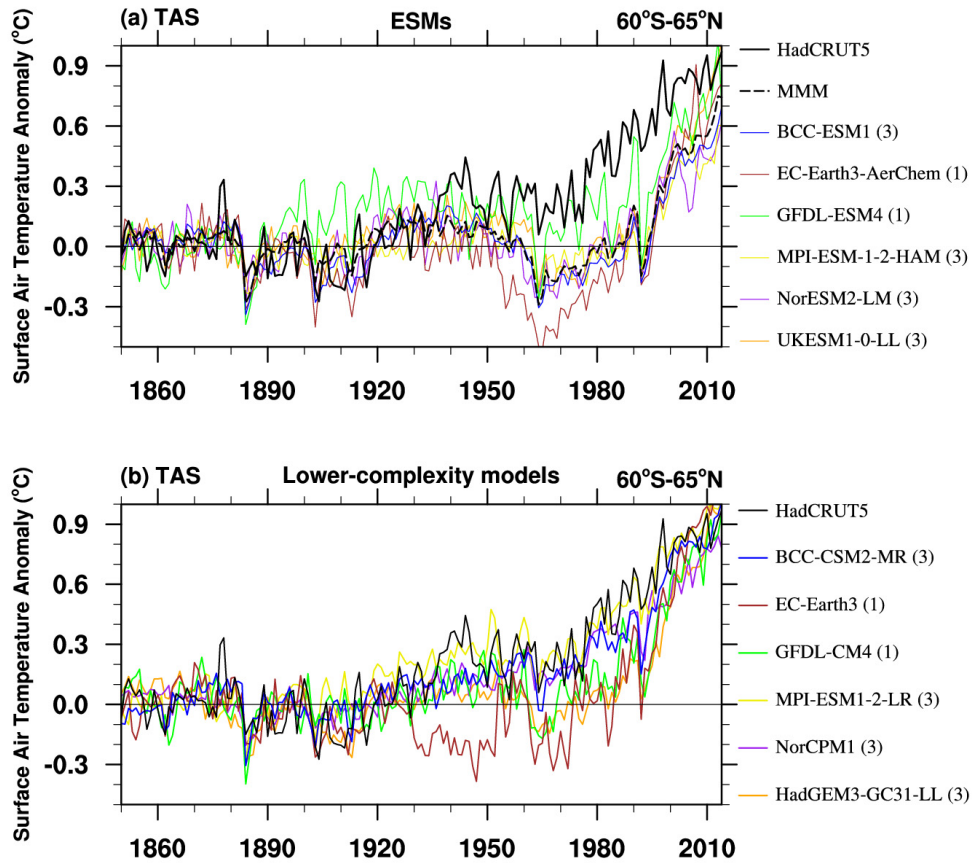
235       Decomposition of the ARI, the cloud-amount term and cloud-albedo term of ACI  
236 are detailed further in the Appendix. The aerosol-cloud feedbacks are mainly in the ACI  
237 term which includes cloud spatial extent (amount), cloud albedo on radiative fluxes,  
238 and cloud particle swelling by humidification (Christensen et al., 2017; Neubauer et al.,  
239 2017). There is also a (smaller) effect of feedback on the ARI term that is also affected  
240 by cloud amount changes insofar as increased/decreased cloud cover can obscure/reveal  
241 clear-sky radiative fluxes. We acknowledge that the linear approximation in our method  
242 doesn't explicitly account for the absorption above clouds, or the adjustments to  
243 aerosol-radiation interactions (e.g., Carslaw et al., 2013) that are known to be locally  
244 important. Our formulation explicitly assumes that there is a broadly linear relationship  
245 between loadSO4 and emissions, and aerosol radiation with loadSO4 (and non-linearity  
246 due to cloud albedo or amount or any interaction is small at global scale as suggested  
247 in Booth et al. (2018)). Should these interaction terms be non-negligible in this analysis,  
248 we still expect the broader attribution of the reasons for the model diversity in  
249 temperature response over the PHC period, either how they simulate aerosol  
250 concentrations or how they simulate the response to this, to generally hold.

251       This decomposition method is an approximate approach designed to be used with  
252 existing simulations, rather than a strict decomposition by dedicated simulations/output  
253 variables not included in CMIP6. It can't tell us precise information about each  
254 interaction and adjustment, but it can give us an indication of why models behave  
255 differently.

256

### 257 **3. The "pot-hole" bias in CMIP6 ESMs**

258



259  
 260  
 261  
 262  
 263  
 264  
 265  
 266

**Figure 1.** (a) Historical near-global mean (60°S to 65°N) surface air temperature (TAS) anomalies relative to 1850-1900 mean from HadCRUT5 (thick black line), the ensemble mean for each ESM (solid color lines), and multi-model mean (MMM, dashed black line). (b) is the same as (a), but for the lower-complexity models. Units: °C. Value in bracket is the number of available members for each model.

267 Figure 1a shows the near-global averaged time series of annual mean TAS  
 268 anomaly relative to 1850 to 1900 in HadCRUT5 during the historical period from 1850  
 269 to 2014, and the ensemble means for each model except for EC-Earth3-AerChem and  
 270 GFDL-ESM4 (where only a single realization is available for the hist-piAer  
 271 experiment). The unforced, long-term drifts in TAS may occur in some of the ESMs,  
 272 as estimated by their control simulation under pre-industrial conditions (Yool et al.,  
 273 2020). We have not accounted for long-term control simulation drifts in our study as  
 274 we are assuming that our focus on inter-decadal scale variability of TAS anomalies is  
 275 likely to be fairly insensitive to any century scale drifts.

276 The TAS anomaly in HadCRUT5 is generally above the baseline climate from the  
277 1940s onwards, and warms fastest from the 1980s to 1990s. Compared with the  
278 observations, all the ESM simulations have negative TAS anomaly biases after the  
279 1940s, which are also evident in the ensemble-mean historical TAS of 25 CMIP6  
280 models with and without interactive chemistry schemes (Flynn and Mauritsen, 2020).  
281 In the ESMs and their ensemble mean (MMM), the cold anomaly biases resemble a  
282 "pot-hole" shape (Fig.1a), which is relatively small before the 1950s and after the 2000s  
283 but prominent from the 1960s to 1990s. To reduce the impact of the change in the spatial  
284 pattern of the emissions in the late 20th century, and the Pinatubo eruption in the early  
285 1990s, we mainly focus on the excessively cold anomaly from 1960 to 1990 in this  
286 study. The impacts from the Agung (1963) and El Chichon (1982) eruptions have been  
287 left in the PHC period as their effect on the simulated temperature is not as pronounced  
288 as the response to Pinatubo and are short-lived in time compared to the period we study.  
289 The period of anomalous cold in the global mean from 1960 to 1990 in model  
290 simulations is defined as the "pot-hole" cooling (PHC). Table 3 shows the TAS  
291 anomaly biases in two periods, the pre-PHC period (1929~1959) and the PHC period  
292 (1960~1990). The cold bias in the MMM is -0.14 in the pre-PHC period and intensified  
293 to -0.40 in the PHC period. The PHC bias ranges from -0.20°C to -0.58°C among the  
294 ESMs with a standard deviation of 0.11°C. Intra-model spread of PHC is relatively  
295 smaller. That is, model structural uncertainty is more responsible for PHC than internal  
296 climate variability.

297

298 **Table 3.** Biases in near-global averaged TAS anomalies relative to 1850-1900 from the  
299 ensemble mean and standard deviation (SD) for each ESM and the corresponding  
300 lower-complexity model in the pre-PHC (1929~1959) and the PHC period. Biases are  
301 relative to the HadCRUT5. The MMM and the SD of the ESMs are shown in the bottom  
302 row. The aerosol effective forcing (ERFaer) is also shown for each ESM. Note that the  
303 relevant fixed-SST simulations to calculate ERF were not available for MPI-ESM-1-2-  
304 HAM.

| ESMs                    | pre-PHC            | PHC                | ERFaer | Lower-complexity models | pre-PHC            | PHC                |
|-------------------------|--------------------|--------------------|--------|-------------------------|--------------------|--------------------|
|                         | Ensemble mean (SD) | Ensemble mean (SD) |        |                         | Ensemble mean (SD) | Ensemble mean (SD) |
| <b>BCC-ESM1</b>         | -0.12<br>(0.01)    | -0.45<br>(0.07)    | -1.47  | <b>BCC-CSM2-MR</b>      | -0.09<br>(0.01)    | -0.10<br>(0.01)    |
| <b>EC-Earth-AerChem</b> | -0.27              | -0.58              | -1.1   | <b>EC-Earth3</b>        | -0.37              | -0.37              |
| <b>GFDL-ESM4</b>        | -0.02              | -0.20              | -0.70  | <b>GFDL-CM4</b>         | -0.12              | -0.26              |
| <b>MPI-ESM1-2-HAM</b>   | -0.16<br>(0.01)    | -0.39<br>(0.03)    | —      | <b>MPI-ESM1-2-LR</b>    | 0.03<br>(0.03)     | 0.01<br>(0.01)     |
| <b>NorESM2-LM</b>       | -0.16<br>(0.04)    | -0.41<br>(0.04)    | -1.21  | <b>NorCPM1</b>          | -0.10<br>(0.03)    | -0.08<br>(0.04)    |
| <b>UKESM1-0-LL</b>      | -0.10<br>(0.09)    | -0.38<br>(0.08)    | -1.1   | <b>HadGEM3-GC31-LL</b>  | -0.16<br>(0.02)    | -0.33<br>(0.03)    |
| <b>MMM</b>              | -0.14<br>(0.08)    | -0.40<br>(0.11)    |        |                         |                    |                    |

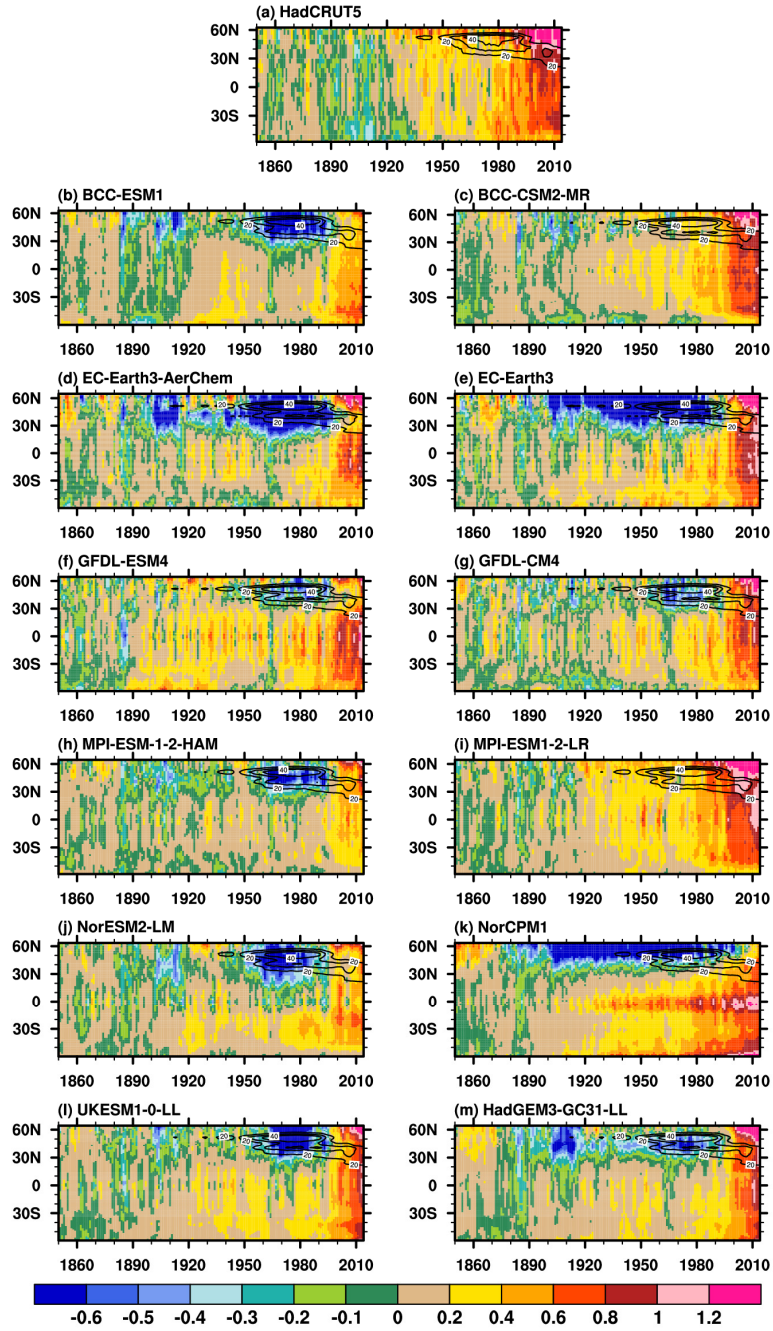
305

306 The PHC bias is generally smaller in the corresponding lower-complexity models  
307 (Fig.1b and Table 3). For models with prescribed chemistry and aerosol (BCC-CSM2-  
308 MR and MPI-ESM1-2-LR), the TAS anomaly are reasonably reproduced during the  
309 pre-PHC period and the PHC period. The PHC bias are large ( $-0.37^{\circ}\text{C}$ ) in EC-Earth3,  
310 which has prescribed chemistry and aerosol. The large bias may be a reflection of the  
311 large internal variability on TAS in EC-Earth3 (Döscher et al., 2021), for which we  
312 have only one member. For models with prescribed chemistry and interactive aerosol  
313 scheme (GFDL-CM4 and HadGEM3-GC31-LL), the cold biases during the PHC  
314 period are comparable with that in the corresponding ESMs.

315 The spatial and temporal evolution of annually averaged TAS anomalies are  
316 further examined (Fig.2). In HadCRUT5, TAS anomalies are generally positive after  
317 the 1940s. The most significant TAS anomalies are evident in the late 20<sup>th</sup> Century and  
318 at the beginning of the 21<sup>st</sup> Century, especially over the NH midlatitudes. The results

319 from BCC-CSM2-MR and MPI-ESM1-2-LR agree well with the observations.  
320 However, the ESMs and the other lower-complexity models simulate pronounced cold  
321 anomalies over NH subtropical-to-high latitudes during the PHC period. The  
322 overestimated tropical and southern hemispheric warming in NorCPM1 offsets most of  
323 the cooling biases over NH subtropical-to-high latitudes.

324         Surface anthropogenic SO<sub>2</sub> emissions rapidly increase during the PHC period (the  
325 line contours in Fig.2). The latitudes of the cooling centers in the ESMs and lower-  
326 complexity models with interactive aerosol scheme are spatially co-located with the  
327 SO<sub>2</sub> emission sources – North America and East Asia (at around 30°N) and Western  
328 Europe (at around 50°N). Generally, the different behaviours seen in Fig.1 and Fig.2  
329 suggest that aerosol forcings may be overestimated in the ESMs and lower-complexity  
330 models with interactive aerosol scheme, and the anomalous cooling is a result of the  
331 extra complexity associated with aerosol processes.

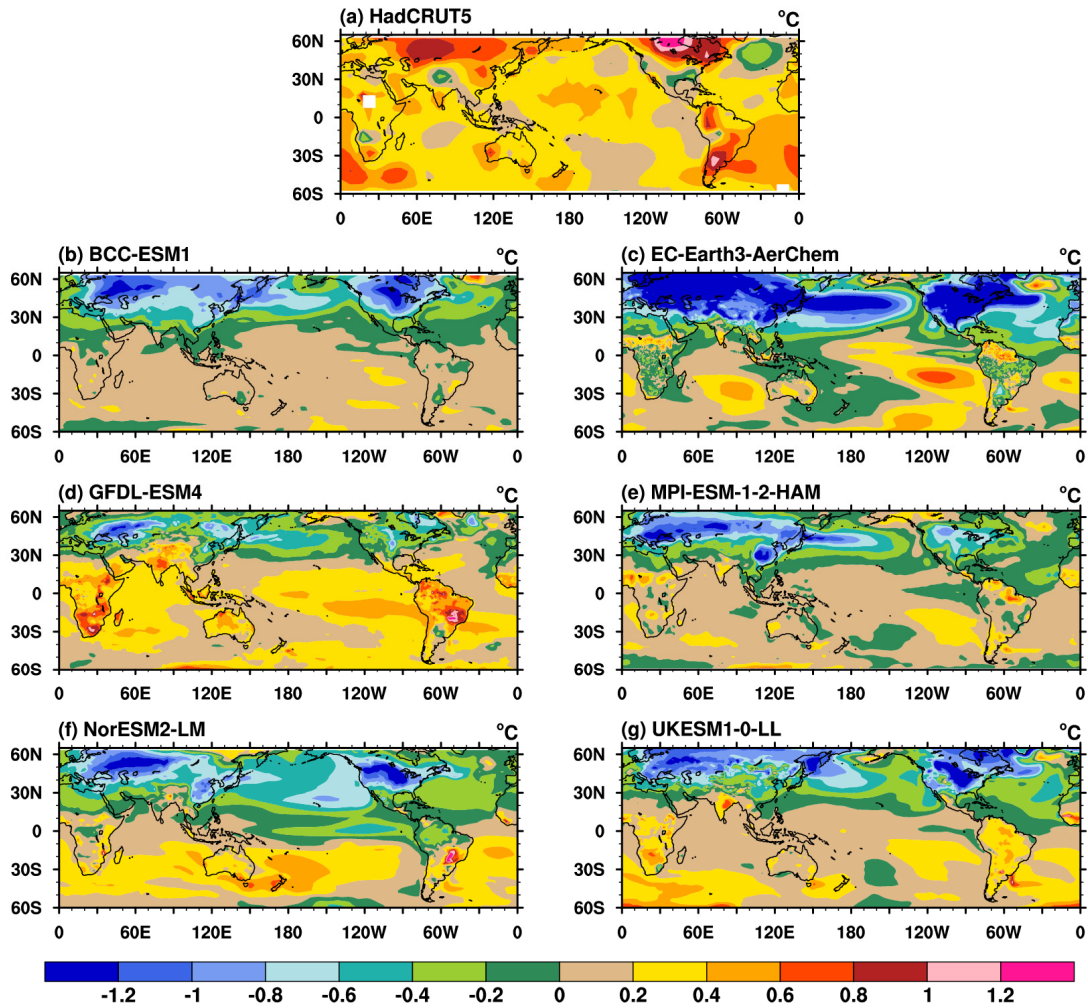


332

333 **Figure 2.** Time-latitude cross-section for annual-mean TAS anomalies (shaded) from (a) HadCRUT5,  
 334 the ensemble mean for each ESM (left panel), and the corresponding lower-complexity model (right  
 335 panel). The anomalies are related to the 1850 ~ 1900 mean. Units: °C. Note that the color scale intervals  
 336 in the positive and negative directions are 0.2 °C and -0.1 °C, respectively. Line contours range from 20  
 337 to 40 ng m<sup>-2</sup> s<sup>-1</sup> with an interval of 10 ng m<sup>-2</sup> s<sup>-1</sup> show the zonal mean anthropogenic surface SO<sub>2</sub> emission  
 338 provided by CMIP6.

339





340

341

342 **Figure 3.** The TAS anomalies during the “pot-hole” period (1960 ~ 1990) from (a) HadCRUT5 and (b-  
 343 g) the ensemble mean for each ESM. The anomalies are relative to the 1850~1900 mean. Units: °C.

344

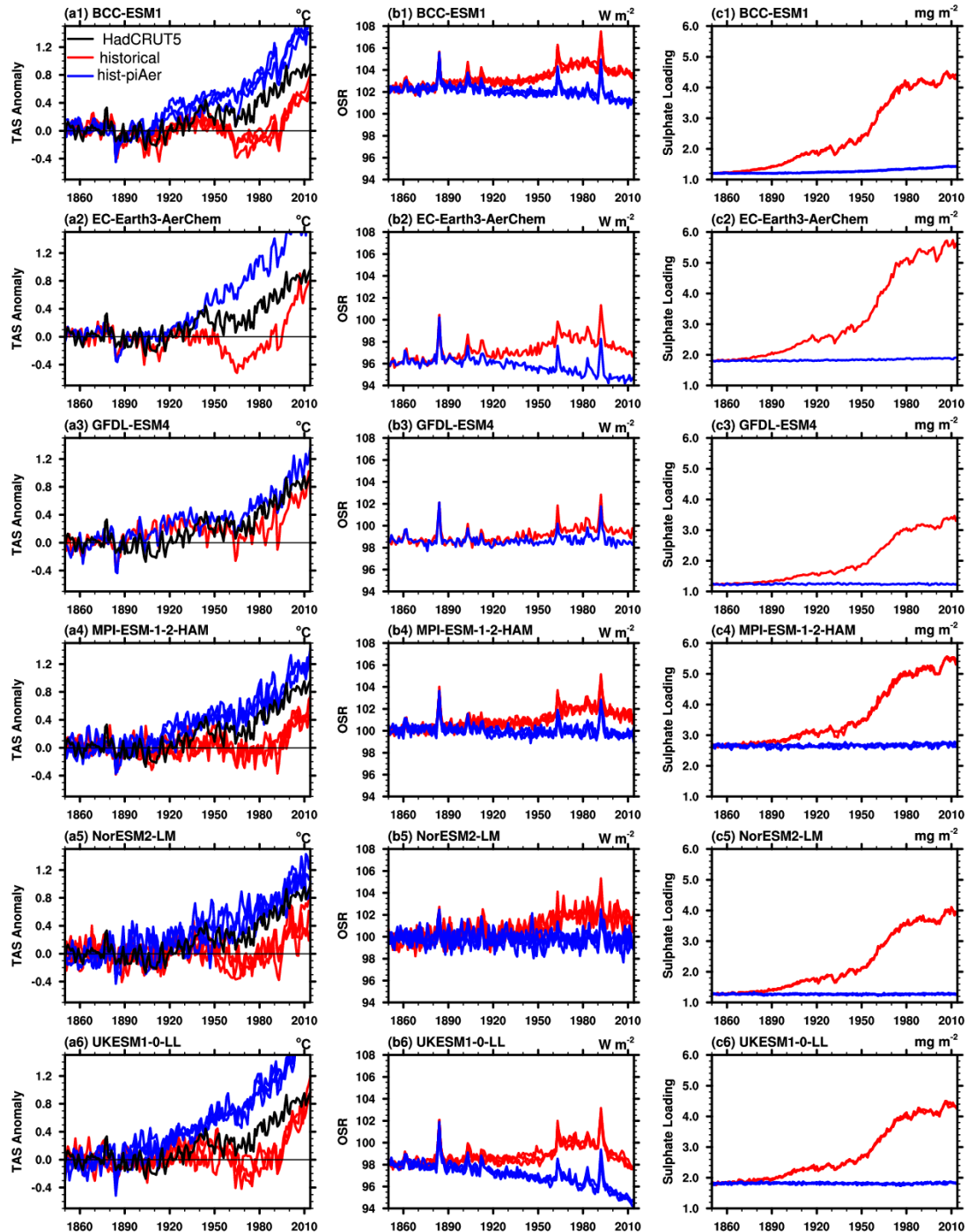
345 During the PHC period. The TAS anomalies in HadCRUT5 are generally positive  
 346 and are the largest over Eurasia and North America (Fig.3a). The warm anomalies are  
 347 on average more than 0.4 °C along the 30°N ~ 60°N latitudinal belt. However, the ESMs  
 348 show anomalies with the opposite sign (Fig.3b-3g) as do the lower-complexity models  
 349 with interactive aerosol scheme (figures not shown). The PHC is pronounced over  
 350 major SO<sub>2</sub> emission centers (Western Europe, East Asia, and the east US) and their  
 351 downstream regions. The cold anomalies over Eurasia and North America are lower  
 352 than -0.6°C in the ESMs. The PHC biases are strongest at lower levels (Figures not  
 353 shown), which is distinct from the amplified upper-tropospheric warming response to

354 greenhouse gases.

355

#### 356 4. Possible reasons for the excessive cooling

357



358

359

360 **Figure 4.** Evolutions of global annual means of (a1-a6) TAS anomalies (left panel, units: °C.), (b1-b6)

361 outgoing shortwave radiation at TOA (OSR, middle panel, units:  $W m^{-2}$ ), and (c1-c6) sulphate loading

362 (right panel, units:  $mg m^{-2}$ ) in HadCRUT5 (black line), each ESM member of the historical (red lines),

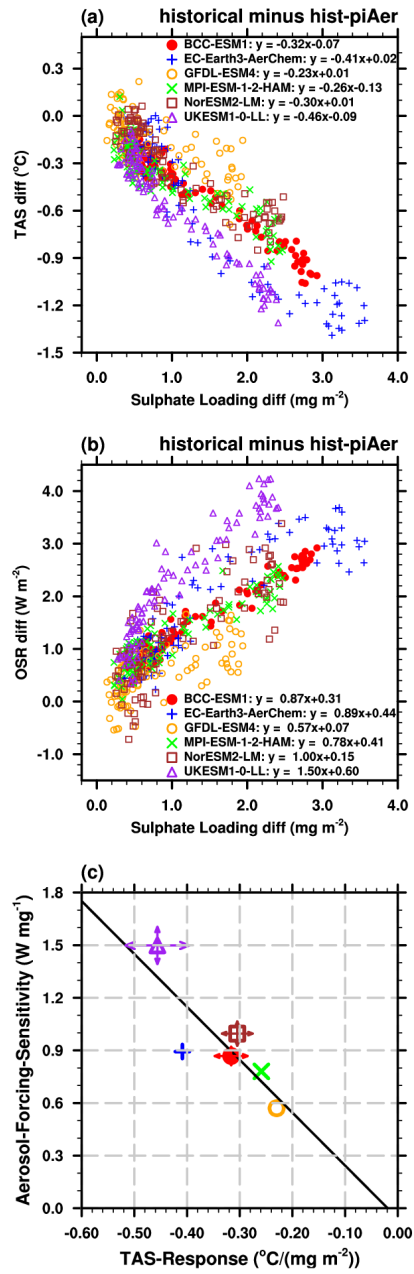
363 and hist-piAer experiments (blue lines). The TAS anomalies are relative to the 1850~1900 mean.

364

365 The differences between the historical and hist-piAer simulations help to  
366 investigate the impact of anthropogenic aerosol emissions and its possible contribution  
367 to the PHC biases. In this section, we examine the TAS, OSR, and sulphate loading  
368 differences, and look in detail at their relationship. As shown by the evolution of TAS  
369 anomalies in the two experiments (Fig.4, left panel), during the PHC period TAS  
370 anomalies in HadCRUT5 (black line) are higher than those in the historical members  
371 but lower than those in the hist-piAer members in all ESMs. That is, the model  
372 responses to anthropogenic aerosol emissions are larger than the amplitude of the PHC.  
373 The temporal evolution of the OSR corresponds with that of the TAS but occurs in the  
374 opposite direction (middle panel). The sulphate loading differences are relatively small  
375 in the 19<sup>th</sup> Century, mildly increase in the first half of the 20<sup>th</sup> Century, grow most  
376 rapidly during the PHC period, and remain high afterward (right panel). The growing  
377 sulphate loading during the PHC period corresponds with the increase in northern-  
378 hemisphere anthropogenic surface SO<sub>2</sub> emissions (line contours in Fig.2). In  
379 comparison with the TAS and OSR differences, the intra-model spread of sulphate  
380 loading for each ESM is relatively small. However, the inter-model diversity of  
381 sulphate loading is large. For example, the sulphate loading difference between the  
382 historical and hist-piAer experiments around the year 2000 is about 4 mg m<sup>-2</sup> in EC-  
383 Earth3-AerChem, almost twice of that in GFDL-ESM4. With similar anthropogenic  
384 SO<sub>2</sub> emission rates, the lower sulphate loading difference in GFDL-ESM4 indicates it  
385 has a shorter sulphate aerosol residence time than that in EC-Earth3-AerChem, which  
386 may be due to their different sulphate production and deposition schemes. The sulphate  
387 loading diversity is also evident in CMIP5 models and is partly responsible for the  
388 diversity in modeled radiative forcing (Wilcox et al., 2015).

389 The latitudinal movement of the SO<sub>2</sub> emission center from the 1990s affects the  
390 relative strength of aerosol forcing. Due to the more rapid oxidation and higher  
391 incoming solar flux at lower latitudes, an equatorward shift in SO<sub>2</sub> emissions around

392 1990s result in a more efficient production of sulphate and stronger aerosol forcing  
393 (Manktelow et al., 2007). The northern mid-latitude temperature is also more sensitive  
394 to the distribution of aerosols, which is approximately twice as large as the global  
395 average (Collins et al., 2013; Shindell and Faluvegi, 2009). Therefore, we focus on the  
396 relationships between TAS, OSR and sulphate loading after 1900 when SO<sub>2</sub> emissions  
397 changes are dominated by its anthropogenic component, and before 1990.. As shown  
398 in Fig.6a, the TAS differences between the historical and hist-piAer simulations vary  
399 approximately linearly with the differences in the sulphate loading. The OSR  
400 differences are approximately linearly correlated with sulphate loading differences  
401 (Fig.6b). In both cases, the approximation of linearity holds less well for UKESM1-0-  
402 LL, especially at small sulphate loadings. This reflects the behaviour of HadGEM2, a  
403 predecessor of UKESM1 (Wilcox et al., 2015), and is likely to be due to the strong  
404 aerosol-cloud albedo effect in these models. The global mean annual mean reff  
405 decreases by about 0.7  $\mu\text{m}$  since pre-industrial era, more than twice the magnitude of  
406 change seen in the other models (Fig.1b in Wilcox et al., 2015 and Fig.9b in this study).



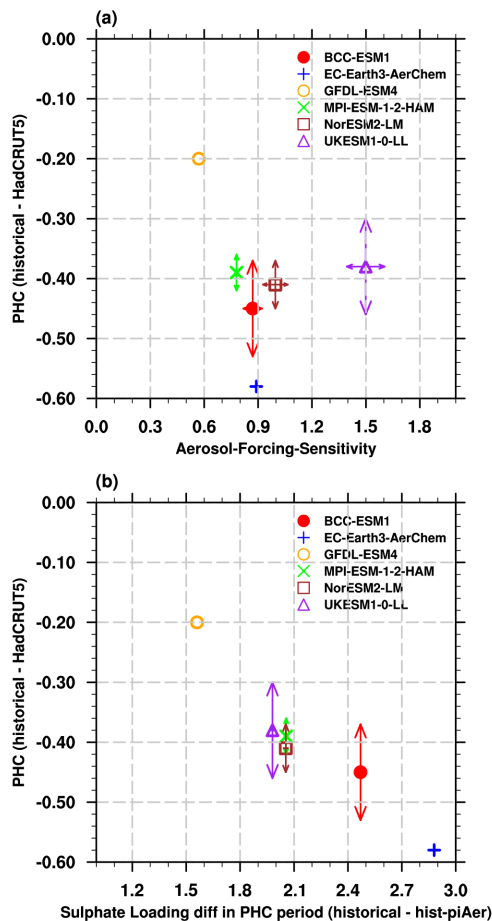
407

408 **Figure 5.** Scatter plots of 1900-1990 yearly sulphate loading differences between the historical and hist-  
 409 piAer simulations (x-axis) versus (a) TAS differences and (b) OSR (y-axis). Results are from the  
 410 ensemble mean for each ESM. The captions are the linear fitting equations. (c) shows the TAS response  
 411 (x-axis) and aerosol-forcing-sensitivity (y-axis) which is equal to slope of linear fitting for each ESM  
 412 (markers), and the corresponding intra-model spread (arrows).

413

414 The slope of the linear fitting equation between TAS (OSR) and sulphate loading  
 415 as shown in the captions in Fig.5a (Fig.5b) is a measure of the sensitivity of TAS  
 416 (aerosol forcing) to perturbations in atmospheric aerosol. Moreover, TAS-response and

417 aerosol-forcing-sensitivity are linearly correlated across the ESMs (Fig.5c). That is, the  
 418 strength of the TAS-response can be understood as the magnitude of aerosol-forcing-  
 419 sensitivity within each ESM. The TAS-response and aerosol-forcing-sensitivity is the  
 420 lowest in GFDL-ESM4. The TAS-response and aerosol-forcing-sensitivity in  
 421 UKESM1-0-LL (the purple marker in Fig.6c) are the strongest, as well as their intra-  
 422 model spread (the length of arrows), indicating that TAS and aerosol forcing in this  
 423 model are relatively more susceptible to changes in aerosol. The aerosol-forcing-  
 424 sensitivity is not correlated with the aerosol effective radiative forcing (ERFaer, Table  
 425 3), largely due to the strong influence of UKESM1-0-LL on the result.



426

427 **Figure 6.** Pot-hole Cooling (PHC) bias in ESMs ( $^{\circ}\text{C}$ ) versus (a) the aerosol-forcing-sensitivity ( $\text{W mg}^{-1}$ )  
 428 and (b) sulphate loading differences ( $\text{mg m}^{-2}$ ) during the PHC period. The arrows show the uncertainty  
 429 ranges among the members in each ESM.

430

431           Considering the close relationship between TAS anomalies and aerosol loading  
432 (Fig.5a), and the impact of aerosol-forcing-sensitivity on the TAS response in ESMs  
433 (Fig.5c), their relative contributions to the PHC biases are examined. Figure 6a shows  
434 the PHC biases versus the aerosol-forcing-sensitivity (markers) and their intra-model  
435 spread (arrows). GFDL-ESM4 has the weakest aerosol-forcing-sensitivity ( $\sim 0.60 \text{ W mg}^{-1}$ )  
436 and the smallest PHC ( $-0.20 \text{ }^\circ\text{C}$ ). However, the relationship between the PHC  
437 biases and the aerosol-forcing-sensitivity among the ESMs is not clear: ESMs have  
438 similar PHC biases (MPI-ESM, NorESM2, and UKESM1) show large differences in  
439 the aerosol-forcing-sensitivity, ranging from  $0.78$  to  $1.5 \text{ W mg}^{-1}$ ; the aerosol-forcing-  
440 sensitivity in EC-Earth3-AerChem is close to that in BCC-ESM1, but the PHC is more  
441 than  $0.1^\circ\text{C}$  lower; the aerosol-forcing-sensitivity in UKESM1-0-LL is the strongest  
442 ( $\sim 1.5 \text{ W mg}^{-1}$ ) but not the PHC bias. Therefore, the aerosol-forcing-sensitivity is not  
443 able to explain the different PHC biases among ESMs.

444           As shown in Fig.6b, the sulphate loading differences between the historical and hist-  
445 piAer experiments during the PHC period are large among ESMs (the X-axis), which  
446 are about  $1.5 \text{ mg m}^{-2}$  in GFDL-ESM4 but approximately  $2.9 \text{ mg m}^{-2}$  in EC-Earth3-  
447 AerChem. The sulphate loading differences during the PHC period and PHC biases  
448 shows a negative correlation: the PHC bias is generally larger in models with higher  
449 sulphate loading over this period; the ESMs with similar PHC biases (MPI-ESM,  
450 NorESM2, and UKESM1) show similar aerosol loading differences. Therefore, the  
451 excessive cooling during the PHC period and the inter-model diversity in ESMs are  
452 attributed to the higher aerosol burden in these models.

## 453 **5. Discussion**

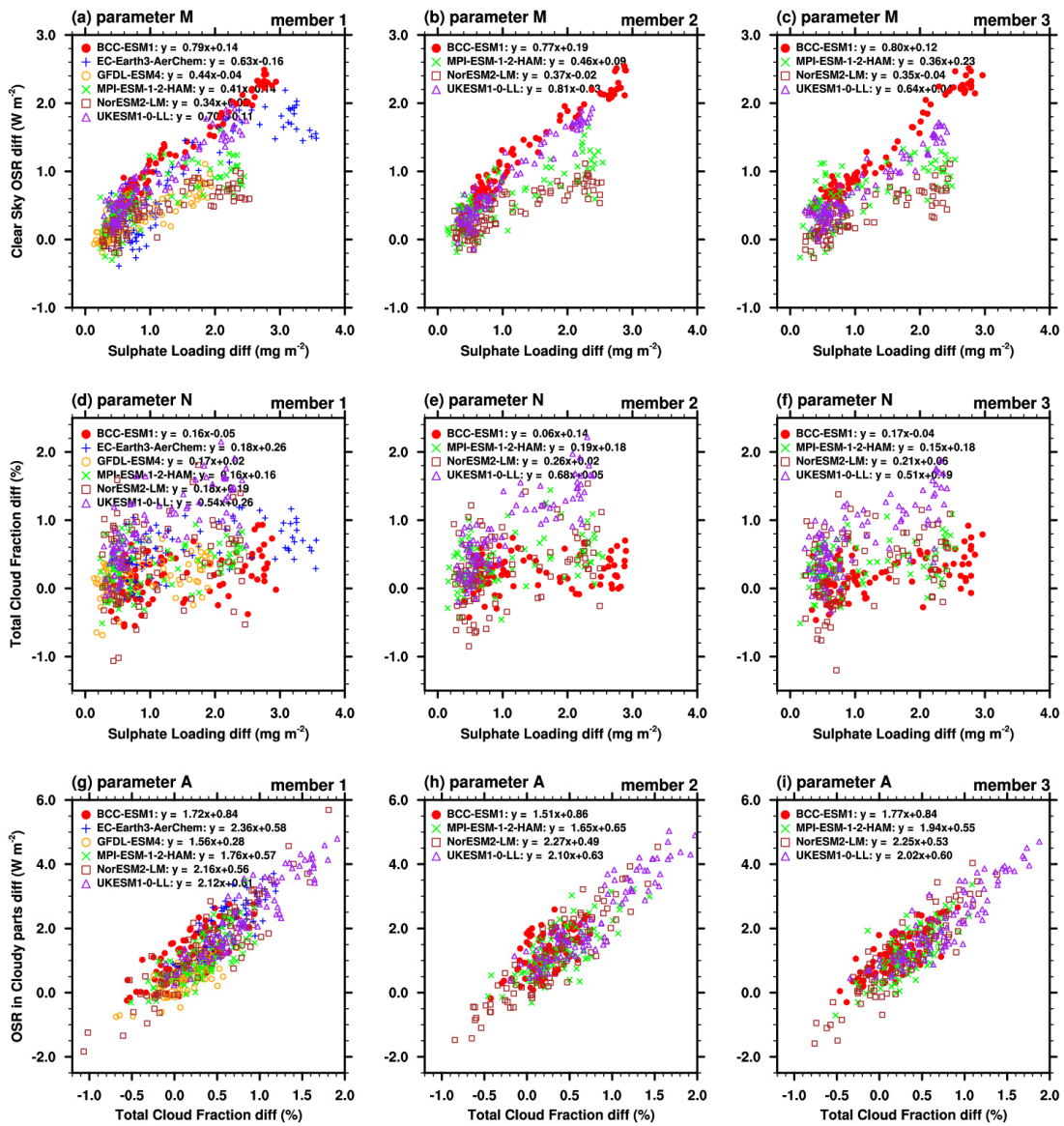
### 454 **5.1 The proportions of ARI and ACI**

455           Although the aerosol-forcing-sensitivity is not responsible for the anomalous  
456 cooling biases in ESMs, it is a good way to identify model differences in the response  
457 to aerosol changes. As shown in Fig.5b, there are significant differences in the aerosol-  
458 forcing-sensitivity among ESMs. The aerosol-forcing-sensitivity in UKESM1-0-L is  
459 almost three times of that in GFDL-ESM4. Due to the uncertainties in physical



460 processes and cloud parameterizations, the dominant component (ARI or ACI) of  
 461 aerosol-forcing-sensitivity may also vary among ESMs. Here, we separate the different  
 462 components of the aerosol-forcing-sensitivity in each ESM by the method introduced  
 463 in the section 2.3 and the Appendix. Sulphate loading is used as a proxy of aerosol  
 464 amount for all aerosol components in the quantification of the total effect because of its  
 465 dominant contribution to anthropogenic aerosol load during this period and its  
 466 covariation with the other aerosol species.

467



468

469 **Figure 7.** Annual mean differences between the historical and hist-piAer simulations in the ESM

470 members during 1900 to 1990 period for (a-c) sulphate loading ( $\text{mg m}^{-2}$ ) versus clear-sky OSR (OSR<sub>clr</sub>,

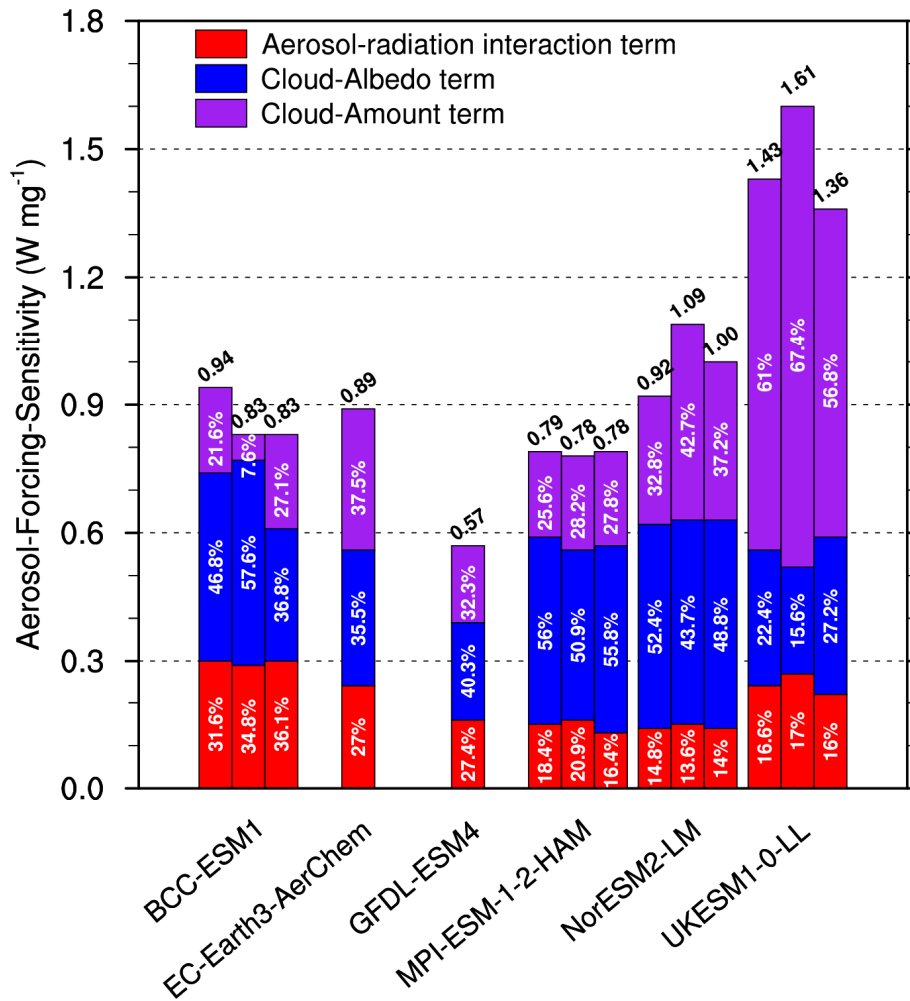


471  $W m^{-2}$ ), (d-f) sulphate loading versus total cloud fraction (%), and (g-i) total cloud fraction versus OSR  
472 in cloudy parts ( $W m^{-2}$ ). Slopes of the linear fitting equations from the top row to the bottom row refer  
473 to the parameters M, N, and A, respectively.

474

475 The ARI can be approximated to  $(1-CLT\_hist/100.) * M$ , where CLT\_hist is cloud  
476 amount in the historical simulation and parameter M is a measure of the strength of  
477 aerosol-radiation interactions ( $\Delta OSR_{clr} / \Delta load_{SO4}$ ). Parameter M varies widely from  
478 about  $0.35 W mg^{-1}$  in NorESM2-LM to about  $0.79 W mg^{-1}$  in BCC-ESM1 (captions in  
479 Fig.7a-7c). Since parameter M does not change much among ensemble members in  
480 each ESM, their ARI is similar across members. That is, the impact of internal climate  
481 variability on the ARI is relatively small, which is consistent with the quantitative  
482 analysis in Fig.8 (Red bars).

483



484

485 **Figure 8.** Total aerosol-forcing-sensitivity from each member in ESMs. The number marked on the top  
 486 is the total aerosol-forcing-sensitivity. Partition of aerosol-radiation interaction term, cloud-albedo term,  
 487 and cloud-amount term are marked in the corresponding color bars. Unit: W mg<sup>-1</sup>. Where multiple  
 488 realizations are available for a model, a bar is shown for each member.

489

490 The ACI can be estimated from the difference between the aerosol-forcing-sensitivity  
 491 and the ARI. The proportion of the aerosol-forcing-sensitivity arising from  
 492 the ACI is higher than 64% in all ESMs (Fig.8). The inter-model variation of the ACI  
 493 (0.37 W mg<sup>-1</sup>) is much larger than that for the ARI (0.09W mg<sup>-1</sup>). For example, the ACI  
 494 in UKESM1-0-LL (~1.2W mg<sup>-1</sup>) is higher than all the others and is about three times  
 495 of that in GFDL-ESM4 (0.41 W mg<sup>-1</sup>). This demonstrates that differences in the  
 496 aerosol-forcing-sensitivity across the ESMs are dominated by the differences in their

497 individual representation of ACI. Chen et al. (2014) also suggested that ACI is the main  
498 contribution to the Aerosol radiative forcing uncertainty and the response of marine  
499 clouds to aerosol changes is paramount. The intra-model variations in the ACI are also  
500 larger than that for the ARI. That is because the intra-model variations of the ACI are  
501 influenced by the effects of climate system internal variability on aerosol-induced cloud  
502 microphysics, with cloud radiative properties and cloud lifetimes varying regionally.  
503 The intra-model variations are also attributable to the differences in atmospheric  
504 circulation among different ensemble members, which may affect the geographical  
505 distributions of aerosols and clouds and lead to a different magnitude of interactions.

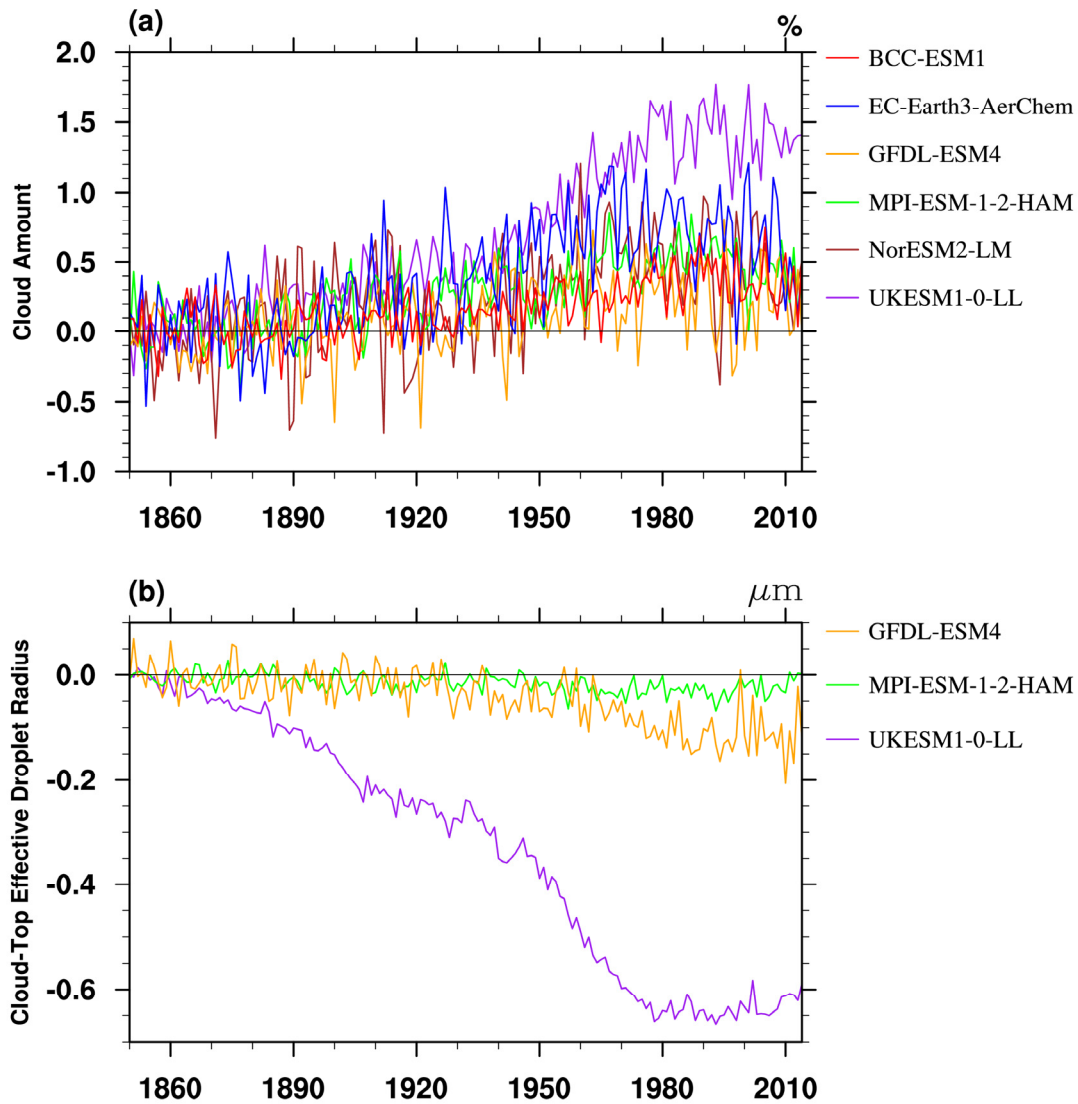
506 The quantitative analysis in Fig.8 also indicates that ESMs with similar aerosol-  
507 forcing-sensitivity may have different contributions from ARI and ACI. The aerosol-  
508 forcing-sensitivity is similar in BCC-ESM1, EC-Earth3-AerChem, MPI-ESM-1-2-  
509 HAM and NorESM2-LM, but the fractional contribution from the ACI is the largest in  
510 NorESM2-LM and its ARI is less than half of that in BCC-ESM1. Generally, BCC-  
511 ESM1 has the largest fractional ARI contribution (34%), whereas NorESM2-LM has  
512 the largest fraction of ACI contribution (86%).

513

## 514 **5.2 The proportions of cloud-amount and cloud-albedo terms**

515 Our ACI metric includes several mechanisms by which aerosols can alter cloud  
516 properties. This includes the cloud-albedo effects (or 'Twomey' effect), referred to as  
517 the radiative forcing part of ACI, and effects of aerosols on the macroscopic properties  
518 of clouds (for example, cloud extent and lifetime), referred to as the adjustments part  
519 of ACI. However, it is complicated to separate these two parts of ACI directly using  
520 available CMIP6 diagnostics, because the former is most accurately defined as a change  
521 in cloud albedo with all other cloud properties held constant (i.e., a change in cloud-  
522 droplet number concentration only), whilst the latter allows cloud properties to respond.

523



524

525

526 **Figure 9** (a) Evolutions of global mean cloud amount differences between the historical and hist-piAer  
 527 simulations in ensemble mean for each ESM, units: %. (b) is the same as (a), but for cloud-top effective  
 528 droplet radius ( $r_{\text{eff}}$ ,  $\mu\text{m}$ ). The  $r_{\text{eff}}$  data is only available for GFDL-ESM4, MPI-ESM-1-2-HAM, and  
 529 UKESM1-0-LL.

530

531 Figure 9 shows the evolution of global-mean differences in total cloud amount  
 532 ( $\Delta\text{CLT}$ ) and cloud-top effective droplet radius ( $\Delta r_{\text{eff}}$ ) between the historical and hist-  
 533 piAer experiments. The  $\Delta\text{CLT}$  and  $\Delta r_{\text{eff}}$  in UKESM1-0-LL are the largest and highly  
 534 correlated with each other (with a correlation coefficient of -0.92 during the 1900 to  
 535 1990 period). For the other two ESMs for which  $\Delta r_{\text{eff}}$  was archived, the correlation

536 coefficient is -0.40 for MPI-ESM-1-2-HAM and insignificant for GFDL-ESM4 (-0.09).  
537 The  $\Delta\text{CLT}$  and  $\Delta r_{\text{eff}}$  differences are smaller in MPI-ESM-1-2-HAM and GFDL-ESM4  
538 than in UKESM1-0-LL, especially for the  $\Delta r_{\text{eff}}$  differences.  $\Delta r_{\text{eff}}$  is generally related to  
539 the cloud-optical depth and cloud water path, and  $\Delta\text{CLT}$  is related to adjustments in  
540 cloud cover due to ACI. Therefore, the radiative forcing part and adjustments part of  
541 ACI may be closely coupled in UKESM1-0-LL and are hard to separate statistically.  
542 The strong correlation between cloud amount and  $r_{\text{eff}}$  response in UKESM1-0-LL  
543 indicates that this model is sensitive to aerosol-cloud interactions, which likely  
544 contributes to it having the strongest aerosol-forcing-sensitivity and intra-model spread  
545 of all the CMIP6 models (Fig.5c). MPI-ESM-1-2-HAM and UKESM1-0-LL have  
546 similar ensemble mean PHC biases and close sulphate burden, but the aerosol-forcing-  
547 sensitivity differences in UKESM1-0-LL is almost twice of that in MPI-ESM-1-2-  
548 HAM (Fig.5). That is, the overestimated sulphate burden dominates the PHC biases,  
549 but the ACI sensitivity may partly affect the amplitude and uncertainty ranges of PHC  
550 biases.

551 Despite of the closely coupled radiative forcing part and adjustments part of ACI  
552 in UKESM1-0-LL, it is still possible to split the ACI into a part that is correlated with  
553 cloud amount differences and a residual term. This can be done statistically by  
554 regressing-out the approximate linear dependence of the differences between historical  
555 and hist-piAer simulations of the cloudy part of OSR ( $\text{OSR}_{\text{cld\_p}}$ ) on cloud fraction in  
556 each ESM (parameter A in Fig.7g-7i). We call the degree of linear correlation of  
557  $\Delta\text{OSR}_{\text{cld\_p}}$  with  $\Delta\text{CLT}$  the "cloud-amount term", and the residual will be referred to  
558 as the "cloud-albedo term". However, we reiterate that the so-called "cloud-amount  
559 term" may also include changes in the reflectivity of clouds if these are correlated with  
560 changes in cloud amount. Similarly, the cloud-albedo term will contain any sources of  
561 cloud amount changes which have not been removed by linearly regressing  $\text{OSR}_{\text{cld\_p}}$   
562 against cloud amount. As such, we do not intend this nomenclature to indicate a precise  
563 separation of the radiative forcing part and adjustments part of ACI. Our decomposition  
564 allows first order assessment of these terms from historical simulations without the need

565 for extra simulations or calls, and also allows estimates from observations and  
566 intermodel comparisons.

567 As described in the section 2.3 and the Appendix, the cloud-amount term is  
568 sensitive to two parameters: the cloud amount response (parameter N in Fig.7d-7f) and  
569 the sensitivity of OSR reflected from clouds to cloud amount changes (parameter A,  
570 Fig.7g-7i). As shown in Fig.8, UKESM1-0-LL has the largest contribution of the cloud-  
571 amount term to aerosol-forcing-sensitivity (62%,  $0.91 \text{ W mg}^{-1}$ ); the cloud-amount term  
572 is the smallest in GFDL-ESM4 ( $\sim 0.18 \text{ W mg}^{-1}$ ). The cloud-albedo term is defined to be  
573 linearly independent of cloud-amount changes (adjustments). For the CMIP6 ESMs, it  
574 can only be estimated as the residual after subtracting the cloud-amount term from the  
575 ACI. The cloud-albedo term is similar in BCC-ESM1, MPI-ESM-1-2-HAM, and  
576 NorESM2-LM. The inter-model variation for the cloud-amount term is about twice of  
577 that for the cloud-albedo term ( $0.29 \text{ W/mg}$  v.s.  $0.16 \text{ W/mg}$ ). That is, the variations of  
578 cloud-amount term are the major source of inter-model ACI (and the aerosol-forcing-  
579 sensitivity) differences between ESMs. Therefore, difference in the cloud-amount  
580 terms, across the ESMs, dominates the uncertainties in the aerosol-forcing-sensitivity.

581 Note that, our definitions do not correspond to the effects measured by using  
582 multiple calls to the radiation scheme of a model, with and without aerosols, which  
583 measure instantaneous radiative effects; multiple calls give a measure of the fast  
584 response of clouds to aerosol perturbations in a fixed thermodynamic and dynamical  
585 background, allowing for a clear separation between ACI and rapid adjustments (e.g.,  
586 Bellouin et al., 2013). This differs from aerosol forcing diagnosed by differencing  
587 climate projections with different aerosol forcings, which include the slow effects of  
588 other feedbacks. For example, differences in climate forcings can lead to different SST  
589 patterns, which in turn alter the location and characteristics of clouds. Despite these  
590 differences, an advantage of our classification is that it provides a possible method for  
591 model evaluation since the variables used are also, in principle, available from the  
592 observations.

593

594 **6. Conclusion**

595 This study focuses on the reproduction of historical surface air temperature  
596 anomalies in six CMIP6 ESMs. The ESMs systematically underestimate TAS  
597 anomalies relative to 1850 to 1900 in the NH midlatitudes, especially from 1960 to  
598 1990, the "pot-hole" cooling (PHC) period. Previous studies suggested that aerosol  
599 cooling is too strong in many CMIP6 models. Our study more specifically found that  
600 the PHC is concurrent in time and space with anthropogenic SO<sub>2</sub> emissions, which  
601 rapidly increase in the PHC period in NH. Models with larger aerosol burdens have  
602 larger PHC biases. The primary role of aerosol emissions in these biases is further  
603 supported by the differences between ESMs and the lower-complexity models with  
604 prescribed aerosol.

605 Differences between historical simulations and simulations with aerosol emissions  
606 fixed at their preindustrial levels (hist-piAer) are used to isolate the impacts of industrial  
607 aerosol emission. We propose that the overestimated aerosol concentrations in the  
608 ESMs are responsible for the spurious drop in TAS in the mid-twentieth century, rather  
609 than a high sensitivity of the models to aerosol forcing. Although the aerosol-forcing-  
610 sensitivity differences in ESMs cannot explain the PHC biases, it is a good  
611 measurement of aerosol effects that can be used to explore structural differences  
612 between models. A simple metric is derived for determining the dominant contribution  
613 to the aerosol-forcing-sensitivity in any specific model: ARI or ACI. The ACI accounts  
614 for more than 64% of the aerosol-forcing-sensitivity in all analyzed ESMs. The  
615 considerable inter-model variation in the aerosol-forcing-sensitivity is mainly  
616 attributable to the uncertainty in the ACI within models. The ACI can be further  
617 decomposed into a cloud-amount term and a cloud-albedo term. The cloud-amount term  
618 is found to be the major source of inter-model diversity of ACI. Considering the crucial  
619 role of cloud properties on the inter-model spread in aerosol-forcing-sensitivity, the  
620 aerosol-cloud interactions should be a focus in development of aerosol schemes within  
621 ESMs.

622

623 **Appendix: Decomposition of the Aerosol-radiation interaction and aerosol-cloud**  
 624 **interaction**

625 Considering the dominant role of sulphate aerosol on anthropogenic aerosol  
 626 forcing, we use the sulphate loading (loadSO4) as a proxy for all aerosol in our analysis.  
 627 The aerosol-forcing-sensitivity (as determined by the difference between the historical  
 628 and hist-piAer experiments) is estimated by the all-sky OSR differences per sulfate  
 629 burden unit ( $\Delta \text{OSR} / \Delta \text{loadSO4}$ ) and it is the combination of OSR differences in the  
 630 clear-sky parts ( $\Delta \text{OSR}_{\text{clr}_p} / \Delta \text{loadSO4}$ ) and the cloudy parts ( $\Delta \text{OSR}_{\text{cld}_p} / \Delta$   
 631  $\text{loadSO4}$ ):

$$632 \quad \Delta \text{OSR} / \Delta \text{loadSO4} = \Delta \text{OSR}_{\text{clr}_p} / \Delta \text{loadSO4} + \Delta \text{OSR}_{\text{cld}_p} / \Delta \text{loadSO4}. \quad (A1)$$

634 The  $\text{OSR}_{\text{clr}_p}$  for a particular experiment can be calculated as:

$$635 \quad \text{OSR}_{\text{clr}_p} = (1 - \text{CLT} / 100.) * \text{OSR}_{\text{clr}}, \quad (A2)$$

636 where CLT is the total cloud amount (unit: %), and  $\text{OSR}_{\text{clr}}$  is the OSR assuming all  
 637 clear sky (unit:  $\text{W}/\text{m}^2$ ). The cloud amount changes ( $\Delta \text{CLT}$ ) will modify the proportion  
 638 of clear-sky and then affect the OSR changes attributed to the clear-sky part by covering  
 639 or uncovering aerosols in clear sky. Therefore, based on equation (A2),  $\Delta \text{OSR}_{\text{clr}_p} / \Delta$   
 640  $\text{loadSO4}$  can be decomposed into the  $\text{OSR}_{\text{clr}}$ -response ( $\Delta \text{OSR}_{\text{clr}} / \Delta \text{loadSO4}$ ) and  
 641 CLT-response ( $\Delta \text{CLT} / \Delta \text{loadSO4}$ ):

$$642 \quad \Delta \text{OSR}_{\text{clr}_p} / \Delta \text{loadSO4} = (1 - \text{CLT}_{\text{hist}} / 100.) * \Delta \text{OSR}_{\text{clr}} / \Delta \text{loadSO4}$$

$$643 \quad - \text{OSR}_{\text{clr}_{\text{hist}}} / 100 * \Delta \text{CLT} / \Delta \text{loadSO4} + \text{residual}_{\text{clr}_p}$$

$$644 \quad = (1 - \text{CLT}_{\text{hist}} / 100.) * M - \text{OSR}_{\text{clr}_{\text{hist}}} / 100 * N + \text{residual}_{\text{clr}}, \quad (A3)$$

645 where  $\text{CLT}_{\text{hist}}$  and  $\text{OSR}_{\text{clr}_{\text{hist}}}$  are the mean CLT and  $\text{OSR}_{\text{clr}}$  in the historical  
 646 experiment.  $\text{Residual}_{\text{clr}}$  is the residual term that is non-linear in  $\Delta \text{OSR}_{\text{clr}}$  and  $\Delta \text{CLT}$ .  
 647 The parameter  $M = \Delta \text{OSR}_{\text{clr}} / \Delta \text{loadSO4}$  is related to strength of aerosol-radiation  
 648 interaction and can be estimated by linear fitting of  $\Delta \text{OSR}_{\text{clr}}$  on  $\Delta \text{loadSO4}$ . The  
 649 parameter  $N = \Delta \text{CLT} / \Delta \text{loadSO4}$  is related to CLT-response and estimated by linear  
 650 fitting of  $\Delta \text{CLT}$  on  $\Delta \text{loadSO4}$ . Therefore, the first term on the right-hand side of Eq.  
 651 (A3),  $(1 - \text{CLT}_{\text{hist}} / 100.) * M$ , corresponds to the aerosol radiative effect; the second term,  
 652  $- \text{OSR}_{\text{clr}_{\text{hist}}} / 100 * N$ , corresponds to the impact of changes in clear-sky area.

653 The  $\text{OSR}_{\text{cld}_p}$  is the cloudy part of OSR, accounting for the difference between  
 654 OSR and  $\text{OSR}_{\text{clr}_p}$ . The cloudy part of the OSR differences ( $\Delta \text{OSR}_{\text{cld}_p}$ ) can be



655 generally estimated as:

$$656 \quad \Delta OSR_{cld\_p} = A * \Delta CLT + \text{cloud-albedo relative changes} + \text{residual\_cld},$$

657 where the parameter  $A = \Delta(OSR - OSR_{clr\_p}) / \Delta CLT$  is the sensitivity of the shortwave  
 658 flux reflected by clouds to changes in cloud amount. The parameter A depends on the  
 659 baseline cloud albedo (radiative flux per cloud amount unit) and can be estimated by  
 660 linear fitting of  $\Delta OSR_{cld\_p}$  on  $\Delta CLT$ . Hence,

$$661 \quad \Delta OSR_{cld\_p} / \Delta loadSO4 = A * \Delta CLT / \Delta loadSO4 + \text{cloud-albedo term}$$

$$662 \quad \quad \quad + \text{residual\_cld},$$

$$663 \quad \quad \quad = A * N + \text{cloud-albedo term} + \text{residual\_cld}, \quad (A4)$$

664

665 where N is the parameter defined above. Therefore, the first term on the right-hand side  
 666 of equation (A4),  $A * N$ , corresponds to the impact of cloud amount changes on the cloud  
 667 radiation; and the cloud-albedo term can be obtained as a residual after subtracting  $A * N$   
 668 from  $\Delta OSR_{cld\_p} / \Delta loadSO4$ , thereby eliminating any linear dependence of the cloudy-  
 669 sky shortwave flux response on cloud-amount changes.

670 As with the clear-sky decomposition, *residual\_cld* is a possible non-linear term and  
 671 is assumed to be small. This term cannot in fact be distinguished from the cloud-albedo  
 672 term, in this analysis: we must therefore accept that cloud-albedo changes could be  
 673 accompanied by non-linear changes in macroscopic cloud properties (in this  
 674 framework).

675 The total aerosol-forcing-sensitivity can be measured by substituting the derived  
 676 values of  $\Delta OSR / \Delta loadSO4$  from both the clear sky (equation A3) and cloudy  
 677 (equation A4) parts back into equation (A1):

$$678 \quad \Delta OSR / \Delta loadSO4 = (1 - CLT_{hist}/100.) * M - OSR_{clr\_hist}/100 * N$$

$$679 \quad \quad \quad + A * N + \text{cloud\_albedo\_term} + \text{residual}$$

$$680 \quad \quad \quad = (1 - CLT_{hist}/100.) * M + (A - OSR_{clr\_hist}/100.) * N$$

$$681 \quad \quad \quad + \text{cloud\_albedo\_term} + \text{residual\_osr}. \quad (A5)$$

682

683 Based on equation (A5), the total aerosol-forcing-sensitivity can therefore be  
 684 decomposed to the aerosol-radiation interaction term (ARI),  $(1 - CLT_{hist}/100.) * M$ ,  
 685 cloud-amount term as  $(A - OSR_{clr\_hist}/100.) * N$  including the impacts of cloud amount  
 686 changes on aerosol radiation  $(-OSR_{clr\_hist}/100.*N)$  and cloud radiation  $(A * N)$ , and  
 687 cloud-albedo term (defined as a residual).

688

689

690 **Data Availability.** All the model data can be freely downloaded from the Earth System  
691 Federation Grid (ESGF) nodes (<https://esgf-node.llnl.gov/search/cmip6/>). The global  
692 historical surface temperature anomalies HadCRUT5 dataset is freely available on  
693 <https://www.metoffice.gov.uk/hadobs/hadcrut5/data/current/download.html>.

694

#### 695 **Author contributions**

696 The main ideas were developed by JZ, KF, STT, JPM, and TW. JZ, KF, and STT wrote  
697 the original draft, and the results were supervised by LJW, BBB, and DS. All the  
698 authors discussed the results and contributed to the final manuscript.

699

#### 700 **Competing interests**

701 The authors declare that they have no conflict of interest.

702

#### 703 **Acknowledgments**

704 This work was supported by The National Key Research and Development Program of  
705 China (Grant no. 2018YFE0196000 and 2016YFA0602100). All the AUTHORS were  
706 supported by the UK-China Research & Innovation Partnership Fund through the Met  
707 Office Climate Science for Service Partnership (CSSP) China as part of the Newton  
708 Fund. LJW was supported by the National Environmental Research Council (NERC)  
709 “North Atlantic Climate System Integrated Study” (ACSIS) program.

710

711 **Reference**

- 712 Aas, W., Mortier, A., Bowersox, V., Cherian, R., Faluvegi, G., Fagerli, H., Hand, J.,  
713 Klimont, Z., Galy-Lacaux, C., Lehmann, C. M. B., Myhre, C. L., Myhre, G., Olivie,  
714 D., Sato, K., Quaas, J., Rao, P. S. P., Schulz, M., Shindell, D., Skeie, R. B., Stein,  
715 A., Takemura, T., Tsyro, S., Vet, R., and Xu, X.: Global and regional trends of  
716 atmospheric sulfur (vol 9, 953, 2019), *Scientific Reports*, 10, 10.1038/s41598-  
717 020-62441-w, 2020.
- 718 ALBRECHT, B. A.: Aerosols, Cloud Microphysics, and Fractional Cloudiness,  
719 *Science*, 245, 1227-1230, 10.1126/science.245.4923.1227, 1989.
- 720 Bellouin, N., Mann, G. W., Woodhouse, M. T., Johnson, C., Carslaw, K. S., and Dalvi,  
721 M.: Impact of the modal aerosol scheme GLOMAP-mode on aerosol forcing in  
722 the Hadley Centre Global Environmental Model, *Atmospheric Chemistry and*  
723 *Physics*, 13, 3027-3044, 10.5194/acp-13-3027-2013, 2013.
- 724 Bethke, I., Wang, Y., Counillon, F., Kimmritz, M., Fransner, F., Samuelsen, A.,  
725 Langehaug, H. R., Chiu, P.-G., Bentsen, M., Guo, C., Tjiputra, J., Kirkevåg, A.,  
726 Olivie, D. J. L., Seland, Ø., Fan, Y., Lawrence, P., Eldevik, T., and Keenlyside,  
727 N.: NCC NorCPM1 model output prepared for CMIP6 CMIP, Earth System Grid  
728 Federation [dataset], 10.22033/ESGF/CMIP6.10843, 2019.
- 729 Bindoff, N. L., Stott, P. A., AchutaRao, K. M., Allen, M. R., Gillett, N., Gutzler, D.,  
730 Hansingo, K., Hegerl, G., et al.: Detection and Attribution of Climate Change:  
731 from Global to Regional, in: *Climate Change 2013: The Physical Science Basis.*  
732 *Contribution of Working Group I to the Fifth Assessment Report of the*  
733 *Intergovernmental Panel on Climate Change* [Stocker, T.F., D. Qin, G.-K. Plattner,  
734 M. Tignor, S.K. Allen, J. Boschung, A. Nauels, Y. Xia, V. Bex and P.M. Midgley  
735 (eds.)]. Cambridge University Press, Cambridge, United Kingdom and New York,  
736 NY, USA.
- 737 Booth, B. B. B., Harris, G. R., Jones, A., Wilcox, L., Hawcroft, M., and Carslaw, K. S.:  
738 Comments on “Rethinking the Lower Bound on Aerosol Radiative Forcing”,  
739 *Journal of Climate*, 31, 9407-9412, 10.1175/jcli-d-17-0369.1, 2018.
- 740 Carslaw, K. S., Lee, L. A., Reddington, C. L., Pringle, K. J., Rap, A., Forster, P. M.,  
741 Mann, G. W., Spracklen, D. V., Woodhouse, M. T., Regayre, L. A., and Pierce, J.  
742 R.: Large contribution of natural aerosols to uncertainty in indirect forcing, *Nature*,  
743 503, 67-71, 10.1038/nature12674, 2013.
- 744 Charlson, R. J., Langner, J., and Rodhe, H.: Sulphate aerosol and climate, *Nature*, 348,  
745 22-22, 10.1038/348022a0, 1990.
- 746 Chen, Y.-C., Christensen, M. W., Stephens, G. L., and Seinfeld, J. H.: Satellite-based  
747 estimate of global aerosol–cloud radiative forcing by marine warm clouds, *Nat.*  
748 *Geosci.*, 7, 643-646, 10.1038/ngeo2214, 2014.
- 749 Christensen, M. W., Neubauer, D., Poulsen, C. A., Thomas, G. E., McGarragh, G. R.,  
750 Povey, A. C., Proud, S. R., and Grainger, R. G.: Unveiling aerosol-cloud  
751 interactions - Part 1: Cloud contamination in satellite products enhances the  
752 aerosol indirect forcing estimate, *Atmospheric Chemistry and Physics*, 17, 13151-  
753 13164, 10.5194/acp-17-13151-2017, 2017.

754 Collins, W., Lamarque, J.-F., Schulz, M., Boucher, O., Eyring, V., Hegglin, M.,  
755 Maycock, A., Myhre, G., Prather, M., Shindell, D., and Smith, S.: AerChemMIP:  
756 Quantifying the effects of chemistry and aerosols in CMIP6, *Geoscientific Model*  
757 *Development*, 10, 585-607, 10.5194/gmd-10-585-2017, 2017.

758 Collins, W. J., Fry, M. M., Yu, H., Fuglestedt, J. S., Shindell, D. T., and West, J. J.:  
759 Global and regional temperature-change potentials for near-term climate forcings,  
760 *Atmospheric Chemistry and Physics*, 13, 2471-2485, 10.5194/acp-13-2471-2013,  
761 2013.

762 Dittus, A. J., Hawkins, E., Wilcox, L. J., Sutton, R. T., Smith, C. J., Andrews, M. B.,  
763 and Forster, P. M.: Sensitivity of Historical Climate Simulations to Uncertain  
764 Aerosol Forcing, *Geophysical Research Letters*, 47, e2019GL085806,  
765 10.1029/2019gl085806, 2020.

766 Döscher, R., Acosta, M., Alessandri, A., Anthoni, P., Arneth, A., Arsouze, T.,  
767 Bergmann, T., Bernadello, R., Bousetta, S., Caron, L.-P., Carver, G., Castrillo, M.,  
768 Catalano, F., Cvijanovic, I., Davini, P., Dekker, E., Doblus-Reyes, F. J., Docquier,  
769 D., Echevarria, P., Fladrich, U., Fuentes-Franco, R., Gröger, M., v. Hardenberg,  
770 J., Hieronymus, J., Karami, M. P., Keskinen, J.-P., Koenigk, T., Makkonen, R.,  
771 Massonnet, F., Ménégoz, M., Miller, P. A., Moreno-Chamarro, E., Nieradzick, L.,  
772 van Noije, T., Nolan, P., O'Donnell, D., Ollinaho, P., van den Oord, G., Ortega,  
773 P., Prims, O. T., Ramos, A., Reerink, T., Rousset, C., Ruprich-Robert, Y., Le Sager,  
774 P., Schmith, T., Schrödner, R., Serva, F., Sicardi, V., Sloth Madsen, M., Smith, B.,  
775 Tian, T., Tourigny, E., Uotila, P., Vancoppenolle, M., Wang, S., Wårlind, D.,  
776 Willén, U., Wyser, K., Yang, S., Yepes-Arbós, X., and Zhang, Q.: The EC-Earth3  
777 Earth System Model for the Climate Model Intercomparison Project 6, *Geosci.*  
778 *Model Dev. Discuss.* [preprint], <https://doi.org/10.5194/gmd-2020-446>, in review,  
779 2021.

780 Dunne, J. P., Horowitz, L. W., Adcroft, A. J., Ginoux, P., Held, I. M., John, J. G.,  
781 Krasting, J. P., Malyshev, S., Naik, V., Paulot, F., Shevliakova, E., Stock, C. A.,  
782 Zadeh, N., Balaji, V., Blanton, C., Dunne, K. A., Dupuis, C., Durachta, J., Dussin,  
783 R., Gauthier, P. P. G., Griffies, S. M., Guo, H., Hallberg, R. W., Harrison, M., He,  
784 J., Hurlin, W., McHugh, C., Menzel, R., Milly, P. C. D., Nikonov, S., Paynter, D.  
785 J., Ploshay, J., Radhakrishnan, A., Rand, K., Reichl, B. G., Robinson, T.,  
786 Schwarzkopf, D. M., Sentman, L. T., Underwood, S., Vahlenkamp, H., Winton,  
787 M., Wittenberg, A. T., Wyman, B., Zeng, Y., and Zhao, M.: The GFDL Earth  
788 System Model Version 4.1 (GFDL-ESM 4.1): Overall Coupled Model Description  
789 and Simulation Characteristics, *J. Adv. Model. Earth Syst.*, 12,  
790 10.1029/2019ms002015, 2020.

791 Eyring, V., Bony, S., Meehl, G. A., Senior, C. A., Stevens, B., Stouffer, R. J., and  
792 Taylor, K. E.: Overview of the Coupled Model Intercomparison Project Phase 6  
793 (CMIP6) experimental design and organization, *Geosci. Model Dev.*, 9, 1937-  
794 1958, 10.5194/gmd-9-1937-2016, 2016.

795 Flynn, C. M. and Mauritsen, T.: On the climate sensitivity and historical warming  
796 evolution in recent coupled model ensembles, *Atmos. Chem. Phys.*, 20, 7829-7842,  
797 10.5194/acp-20-7829-2020, 2020.

798 Gillett, N. P., Shiogama, H., Funke, B., Hegerl, G., Knutti, R., Matthes, K., Santer, B.  
799 D., Stone, D., and Tebaldi, C.: The Detection and Attribution Model  
800 Intercomparison Project (DAMIP v1.0) contribution to CMIP6, *Geosci. Model*  
801 *Dev.*, 9, 3685-3697, 10.5194/gmd-9-3685-2016, 2016.

802 Held, I. M., Guo, H., Adcroft, A., Dunne, J. P., Horowitz, L. W., Krasting, J.,  
803 Shevliakova, E., Winton, M., Zhao, M., Bushuk, M., Wittenberg, A. T., Wyman,  
804 B., Xiang, B., Zhang, R., Anderson, W., Balaji, V., Donner, L., Dunne, K.,  
805 Durachta, J., Gauthier, P. P. G., Ginoux, P., Golaz, J. C., Griffies, S. M., Hallberg,  
806 R., Harris, L., Harrison, M., Hurlin, W., John, J., Lin, P., Lin, S. J., Malyshev, S.,  
807 Menzel, R., Milly, P. C. D., Ming, Y., Naik, V., Paynter, D., Paulot, F.,  
808 Rammaswamy, V., Reichl, B., Robinson, T., Rosati, A., Seman, C., Silvers, L. G.,  
809 Underwood, S., and Zadeh, N.: Structure and Performance of GFDL's CM4.0  
810 Climate Model, *J. Adv. Model. Earth Syst.*, 11, 3691-3727,  
811 10.1029/2019ms001829, 2019.

812 Hoesly, R. M. et al. Historical (1750–2014) anthropogenic emissions of reactive gases  
813 and aerosols from the Community Emissions Data System (CEDS). *Geosci. Model*  
814 *Dev.* 11, 369–408 (2018).

815 Kennedy, J. J., Rayner, N. A., Atkinson, C. P., and Killick, R. E.: An Ensemble Data  
816 Set of Sea Surface Temperature Change From 1850: The Met Office Hadley  
817 Centre HadSST.4.0.0.0 Data Set, *Journal of Geophysical Research-Atmospheres*,  
818 124, 7719-7763, 10.1029/2018jd029867, 2019.

819 Lohmann, U. and Feichter, J.: Global indirect aerosol effects: a review, *Atmospheric*  
820 *Chemistry and Physics*, 5, 715-737, 10.5194/acp-5-715-2005, 2005.

821 Manktelow, P. T., Mann, G. W., Carslaw, K. S., Spracklen, D. V., and Chipperfield, M.  
822 P.: Regional and global trends in sulfate aerosol since the 1980s, *Geophysical*  
823 *Research Letters*, 34, 10.1029/2006gl028668, 2007.

824 Mauritsen, T., Bader, J., Becker, T., Behrens, J., Bittner, M., Brokopf, R., Brovkin, V.,  
825 Claussen, M., Crueger, T., Esch, M., Fast, I., Fiedler, S., Flaeschner, D., Gayler,  
826 V., Giorgetta, M., Goll, D. S., Haak, H., Hagemann, S., Hedemann, C.,  
827 Hohenegger, C., Ilyina, T., Jahns, T., Jimenez-de-la-Cuesta, D., Jungclaus, J.,  
828 Kleinen, T., Kloster, S., Kracher, D., Kinne, S., Kleberg, D., Lasslop, G.,  
829 Kornblueh, L., Marotzke, J., Matei, D., Meraner, K., Mikolajewicz, U., Modali,  
830 K., Moebis, B., Muellner, W. A., Nabel, J. E. M. S., Nam, C. C. W., Notz, D.,  
831 Nyawira, S.-S., Paulsen, H., Peters, K., Pincus, R., Pohlmann, H., Pongratz, J.,  
832 Popp, M., Raddatz, T. J., Rast, S., Redler, R., Reick, C. H., Rohrschneider, T.,  
833 Schemann, V., Schmidt, H., Schnur, R., Schulzweida, U., Six, K. D., Stein, L.,  
834 Stemmler, I., Stevens, B., von Storch, J.-S., Tian, F., Voigt, A., Vrese, P., Wieners,  
835 K.-H., Wilkenskjaeld, S., Winkler, A., and Roeckner, E.: Developments in the MPI-  
836 M Earth System Model version 1.2 (MPI-ESM1.2) and Its Response to Increasing  
837 CO<sub>2</sub>, *J. Adv. Model. Earth Syst.*, 11, 998-1038, 10.1029/2018ms001400, 2019.

838 Meehl, G. A., Senior, C. A., Eyring, V., Flato, G., Lamarque, J.-F., Stouffer, R. J.,  
839 Taylor, K. E., and Schlund, M.: Context for interpreting equilibrium climate  
840 sensitivity and transient climate response from the CMIP6 Earth system models,  
841 *Science Advances*, 6, 10.1126/sciadv.aba1981, 2020.

842 Mitchell, J. F. B., Johns, T. C., Gregory, J. M., and Tett, S. F. B.: Climate response to  
843 increasing levels of greenhouse gases and sulphate aerosols, *Nature*, 376, 501-504,  
844 10.1038/376501a0, 1995.

845 Morice, C. P., Kennedy, J. J., Rayner, N. A., Winn, J. P., Hogan, E., Killick, R. E.,  
846 Dunn, R. J. H., Osborn, T. J., Jones, P. D., and Simpson, I. R.: An Updated  
847 Assessment of Near-Surface Temperature Change From 1850: The HadCRUT5  
848 Data Set, *Journal of Geophysical Research-Atmospheres*, 126,  
849 10.1029/2019jd032361, 2021.

850 Myhre, G., D. Shindell, F.-M. Bréon, W. Collins, J. Fuglestedt, J. Huang, D. Koch, J.-  
851 F. Lamarque, D. Lee, B. Mendoza, T. Nakajima, A. Robock, G. Stephens, T.  
852 Takemura and H. Zhang: Anthropogenic and Natural Radiative Forcing, in:  
853 *Climate Change 2013: The Physical Science Basis. Contribution of Working*  
854 *Group I to the Fifth Assessment Report of the Intergovernmental Panel on Climate*  
855 *Change* [Stocker, T.F., D. Qin, G.-K. Plattner, M. Tignor, S.K. Allen, J. Boschung,  
856 A. Nauels, Y. Xia, V. Bex and P.M. Midgley (eds.)]. Cambridge University Press,  
857 Cambridge, United Kingdom and New York, NY, USA.

858 Neubauer, D., Christensen, M. W., Poulsen, C. A., and Lohmann, U.: Unveiling  
859 aerosol-cloud interactions - Part 2: Minimising the effects of aerosol swelling and  
860 wet scavenging in ECHAM6-HAM2 for comparison to satellite data, *Atmospheric*  
861 *Chemistry and Physics*, 17, 13165-13185, 10.5194/acp-17-13165-2017, 2017.

862 Neubauer, D., Ferrachat, S., Siegenthaler-Le Drian, C., Stoll, J., Folini, D. S., Tegen, I.,  
863 Wieners, K.-H., Mauritsen, T., Stemmler, I., Barthel, S., Bey, I., Daskalakis, N.,  
864 Heinold, B., Kokkola, H., Partridge, D., Rast, S., Schmidt, H., Schutgens, N.,  
865 Stanelle, T., Stier, P., Watson-Parris, D., and Lohmann, U.: HAMMOZ-  
866 Consortium MPI-ESM1.2-HAM model output prepared for CMIP6 AerChemMIP,  
867 Earth System Grid Federation [dataset], 10.22033/ESGF/CMIP6.1621, 2019.

868 Noije, T., Bergman, T., Sager, P., O'Donnell, D., Makkonen, R., Gonçalves-Ageitos,  
869 M., Döscher, R., Fladrich, U., Hardenberg, J., Keskinen, J.-P., Korhonen, H.,  
870 Laakso, A., Myriokefalitakis, S., Ollinaho, P., Pérez García-Pando, C., Reerink,  
871 T., Schrödner, R., Wyser, K., and Yang, S.: EC-Earth3-AerChem, a global climate  
872 model with interactive aerosols and atmospheric chemistry participating in CMIP6,  
873 10.5194/gmd-2020-413, 2020.

874 Osborn, T. J., Jones, P. D., Lister, D. H., Morice, C. P., Simpson, I. R., Winn, J. P.,  
875 Hogan, E., and Harris, I. C.: Land Surface Air Temperature Variations Across the  
876 Globe Updated to 2019: The CRUTEM5 Data Set, *Journal of Geophysical*  
877 *Research: Atmospheres*, 126, e2019JD032352,  
878 <https://doi.org/10.1029/2019JD032352>, 2021.

879 Ramanathan, V. and Feng, Y.: Air Pollution, Greenhouse Gases and Climate Change:  
880 Global and Regional Perspectives, *Atmospheric Environment*, 43, 37-50,  
881 10.1016/j.atmosenv.2008.09.063, 2009.

882 Seland, Ø., Bentsen, M., Olivíe, D., Toniazzo, T., Gjermundsen, A., Graff, L. S.,  
883 Debernard, J. B., Gupta, A. K., He, Y.-C., Kirkevåg, A., Schwinger, J., Tjiputra,  
884 J., Aas, K. S., Bethke, I., Fan, Y., Griesfeller, J., Grini, A., Guo, C., Ilicak, M.,  
885 Karset, I. H. H., Landgren, O., Liakka, J., Moseid, K. O., Nummelin, A.,

886 Spensberger, C., Tang, H., Zhang, Z., Heinze, C., Iversen, T., and Schulz, M.:  
887 Overview of the Norwegian Earth System Model (NorESM2) and key climate  
888 response of CMIP6 DECK, historical, and scenario simulations, *Geosci. Model*  
889 *Dev.*, 13, 6165–6200, <https://doi.org/10.5194/gmd-13-6165-2020>, 2020.

890 Sellar, A. A., Jones, C. G., Mulcahy, J. P., Tang, Y., Yool, A., Wiltshire, A., O'Connor,  
891 F. M., Stringer, M., Hill, R., Palmieri, J., Woodward, S., de Mora, L., Kuhlbrodt,  
892 T., Rumbold, S. T., Kelley, D. I., Ellis, R., Johnson, C. E., Walton, J., Abraham,  
893 N. L., Andrews, M. B., Andrews, T., Archibald, A. T., Berthou, S., Burke, E.,  
894 Blockley, E., Carslaw, K., Dalvi, M., Edwards, J., Folberth, G. A., Gedney, N.,  
895 Griffiths, P. T., Harper, A. B., Hendry, M. A., Hewitt, A. J., Johnson, B., Jones,  
896 A., Jones, C. D., Keeble, J., Liddicoat, S., Morgenstern, O., Parker, R. J., Predoi,  
897 V., Robertson, E., Siahahan, A., Smith, R. S., Swaminathan, R., Woodhouse, M. T.,  
898 Zeng, G., and Zerroukat, M.: UKESM1: Description and Evaluation of the UK  
899 Earth System Model, *J. Adv. Model. Earth Syst.*, 11, 4513-4558,  
900 10.1029/2019ms001739, 2019.

901 Shindell, D. and Faluvegi, G.: Climate response to regional radiative forcing during the  
902 twentieth century, *Nat. Geosci.*, 2, 294-300, 10.1038/ngeo473, 2009.

903 Smith, C. J., Kramer, R. J., Myhre, G., Alterskjaer, K., Collins, W., Sima, A., Boucher,  
904 O., Dufresne, J.-L., Nabat, P., Michou, M., Yukimoto, S., Cole, J., Paynter, D.,  
905 Shiogama, H., O'Connor, F. M., Robertson, E., Wiltshire, A., Andrews, T.,  
906 Hannay, C., Miller, R., Nazarenko, L., Kirkevåg, A., Olivie, D., Fiedler, S.,  
907 Lewinschal, A., Mackallah, C., Dix, M., Pincus, R., and Forster, P. M.: Effective  
908 radiative forcing and adjustments in CMIP6 models, *Atmospheric Chemistry and*  
909 *Physics*, 20, 9591-9618, 10.5194/acp-20-9591-2020, 2020.

910 Stevens, B., Fiedler, S., Kinne, S., Peters, K., Rast, S., Muesse, J., Smith, S. J., and  
911 Mauritsen, T.: MACv2-SP: a parameterization of anthropogenic aerosol optical  
912 properties and an associated Twomey effect for use in CMIP6, *Geoscientific*  
913 *Model Development*, 10, 433-452, 10.5194/gmd-10-433-2017, 2017.

914 Thorne, P. W., Lanzante, J. R., Peterson, T. C., Seidel, D. J., and Shine, K. P.:  
915 Tropospheric temperature trends: history of an ongoing controversy, *Wiley*  
916 *Interdisciplinary Reviews-Climate Change*, 2, 66-88, 10.1002/wcc.80, 2011.

917 Wang, Z., Lin, L., Xu, Y., Che, H., Zhang, X., Zhang, H., Dong, W., Wang, C., Gui,  
918 K., and Xie, B.: Incorrect Asian aerosols affecting the attribution and projection  
919 of regional climate change in CMIP6 models, *Npj Climate and Atmospheric*  
920 *Science*, 4, 10.1038/s41612-020-00159-2, 2021.

921 Weart, S.: *The Discovery of Global Warming*, Bibliovault OAI Repository, the  
922 University of Chicago Press, 9, 10.2307/3986102, 2008.

923 Wilcox, L. J., Highwood, E. J., and Dunstone, N. J.: The influence of anthropogenic  
924 aerosol on multi-decadal variations of historical global climate, *Environmental*  
925 *Research Letters*, 8, 10.1088/1748-9326/8/2/024033, 2013.

926 Wilcox, L. J., Highwood, E. J., Booth, B. B. B., and Carslaw, K. S.: Quantifying sources  
927 of inter-model diversity in the cloud albedo effect, *Geophysical Research Letters*,  
928 42, 1568-1575, 10.1002/2015gl063301, 2015.

929 Williams, K., Copesey, D., Blockley, E., Bodas-Salcedo, A., Calvert, D., Comer, R.,

930 Davis, P., Graham, T., Hewitt, H., Hill, R., Hyder, P., Ineson, S., Johns, T., Keen,  
931 B., Lee, R., Megann, A., Milton, S., Rae, J., Roberts, M., and Xavier, P.: The Met  
932 Office Global Coupled Model 3.0 and 3.1 (GC3.0 and GC3.1) Configurations, *J.*  
933 *Adv. Model. Earth Syst.*, 10, 10.1002/2017MS001115, 2017.

934 Wu, P., Christidis, N., and Stott, P.: Anthropogenic impact on Earth's hydrological  
935 cycle, *Nature Climate Change*, 3, 807-810, 10.1038/nclimate1932, 2013.

936 Wu, T., Hu, A., Gao, F., Zhang, J., and Meehl, G.: New insights into natural variability  
937 and anthropogenic forcing of global/regional climate evolution, *npj Climate and*  
938 *Atmospheric Science*, 2, 10.1038/s41612-019-0075-7, 2019a.

939 Wu, T., Zhang, F., Zhang, J., Jie, W., Zhang, Y., Wu, F., Li, L., Yan, J., Liu, X., Lu,  
940 X., Tan, H., Zhang, L., Wang, J., and Hu, A.: Beijing Climate Center Earth System  
941 Model version 1 (BCC-ESM1): model description and evaluation of aerosol  
942 simulations, *Geosci. Model Dev.*, 13, 977-1005, 10.5194/gmd-13-977-2020, 2020.

943 Wu, T., Lu, Y., Fang, Y., Xin, X., Li, L., Li, W., Jie, W., Zhang, J., Liu, Y., Zhang, L.,  
944 Zhang, F., Zhang, Y., Wu, F., Li, J., Chu, M., Wang, Z., Shi, X., Liu, X., Wei, M.,  
945 Huang, A., Zhang, Y., and Liu, X.: The Beijing Climate Center Climate System  
946 Model (BCC-CSM): the main progress from CMIP5 to CMIP6, *Geosci. Model*  
947 *Dev.*, 12, 1573-1600, 10.5194/gmd-12-1573-2019, 2019b.

948 Yool, A., Palmieri, J., Jones, C. G., Sellar, A. A., de Mora, L., Kuhlbrodt, T., Popova,  
949 E. E., Mulcahy, J. P., Wiltshire, A., Rumbold, S. T., Stringer, M., Hill, R. S. R.,  
950 Tang, Y., Walton, J., Blaker, A., Nurser, A. J. G., Coward, A. C., Hirschi, J.,  
951 Woodward, S., Kelley, D. I., Ellis, R., and Rumbold-Jones, S.: Spin-up of UK  
952 Earth System Model 1 (UKESM1) for CMIP6, *J. Adv. Model. Earth Syst.*, 12,  
953 10.1029/2019ms001933, 2020.

954 Zhang, J., Wu, T., Zhang, F., Furtado, K., Xin, X., Shi, X., Li, J., Chu, M., Zhang, L.,  
955 Liu, Q., Yan, J., Wei, M., and Ma, Q.: BCC-ESM1 Model Datasets for the CMIP6  
956 Aerosol Chemistry Model Intercomparison Project (AerChemMIP), *Advances in*  
957 *Atmospheric Sciences*, 38, 317-328, 10.1007/s00376-020-0151-2, 2021.